vehicles

MDPI

Article

Thermoelastic Modeling of Self-Energizing Carbon-Carbon (C/C) Wedge Brakes for High-Performance Race Vehicles

Giacomo Galvanini [1], Massimiliano Gobbi [1], Giampiero Mastinu [1,*], Carlo Cantoni [2] and Raffaello Passoni [2]

[1] Department of Mechanical Engineering, Politecnico di Milano, Via La Masa, 1, 20156 Milan, Italy; giacomo.galvanini@polimi.it (G.G.); massimiliano.gobbi@polimi.it (M.G.)
[2] Brembo S.p.A, Via Brembo, 25, 24035 Bergamo, Italy; carlo.cantoni@brembo.com (C.C.); raffaello.passoni@brembo.com (R.P.)
* Correspondence: gianpiero.mastinu@polimi.it

Abstract

This study investigates amplified hydraulic braking systems employed in high-performance motorsport applications, utilizing wedge mechanisms for self-energization. An analytical expression for the gain coefficient is derived from a simplified equilibrium analysis of the wedge-shaped pad, capturing the nonlinear dependency on both wedge angle and effective mean disc-pad friction. A previously validated coupled thermoelastic model for carbon-carbon (C/C) braking systems—developed in Dymola and Modelica using the finite volume method (FVM) and an analytical local friction formulation—is here adapted to wedge-amplified braking systems, with the aim of providing performance assessment during the design phase of new calipers at reduced computational cost compared to coupled thermoelastic finite element method (FEM) models. Several caliper configurations featuring different wedge angles are tested experimentally on a dynamometer. A reduction in the effective friction coefficient at high mean effective contact pressure—induced by pronounced wedge angles and reduced pad areas—is observed. To validate the thermoelastic model, simulated braking torque and disc surface temperature are compared against bench data. The model shows satisfactory predictive capability under various operating conditions and test cycles, with mean error indices on peak torque prediction below 5% for the majority of the simulated cases. Finally, the validated model is used to virtually assess the performance of a new caliper prototype prior to its manufacturing and testing.

Keywords: wedge brakes; self-energizing brakes; braking systems; thermoelasticity; carbon-carbon; C/C; finite volume method; Dymola; Modelica

Check for updates

Received: 17 January 2026
Revised: 5 March 2026
Accepted: 6 March 2026
Published: 10 March 2026

Copyright: © 2026 by the authors. Licensee MDPI, Basel, Switzerland. This article is an open access article distributed under the terms and conditions of the Creative Commons Attribution (CC BY) license.

1. Introduction

Braking systems—from a general perspective—are key safety subsystems in ground vehicles, as their primary function is to reduce vehicle speed and, ultimately, bring the vehicle to a safe stop [1]. There are different ways to achieve this braking effect. In internal combustion engine (ICE) vehicles, the most common solution is to dissipate kinetic energy into heat through friction. In contrast, in hybrid electric vehicles (HEVs) and battery electric vehicles (EVs), regenerative braking is employed: electric motors act as generators, converting kinetic energy into electrical energy [1]. Conventional friction brakes, either disc brakes or drum types, rely on the frictional forces that develop at the interface between a stationary component (i.e., the stator) and a rotating component fixed to the wheel (i.e., the rotor). Referring to a conventional friction braking system, its internal gain is defined

as the ratio of the total braking force to the normal clamping force applied by the stator to the rotor [2]. According to this definition, the internal gain of a standard disc brake with two friction surfaces equals twice the mean friction coefficient on the contact area between the disc and the pads [1].

In the literature, self-energizing mechanisms have been proposed as an effective way to increase the internal gain of disc brakes. These systems exploit the tangential braking force itself to push the pads further against the disc, resulting in a form of energy recirculation that improves braking efficiency [3].

A self-energizing solution currently used in disc brakes involves the use of wedge-shaped pads and calipers, as schematically illustrated in Figure 1. In standard calipers, the tangential force generated by friction on the pad under braking is transferred to the caliper through a tangential support surface that is orthogonal to the disc plane (i.e., $\alpha = 90°$, see Figure 1). By reducing the angle α below 90°, a self-energizing wedge effect is introduced. This creates an additional axial force component, which adds to the primary actuation force F_m, resulting in a wedge-amplified braking effect (i.e., amplified caliper).

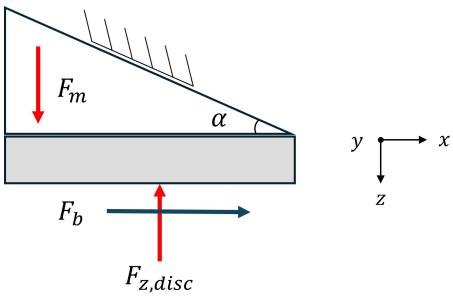

Figure 1. Wedge caliper scheme with actuation force along the normal direction, adapted from [3]. F_m is the actuation force, $F_{z,disc}$ is the resulting total normal force, and F_b is the tangential braking force.

Several examples of wedge caliper solutions have been presented in the literature for road vehicle applications that feature electric or hydraulic actuation. One of the first models, known as eBrake®, was developed by the German Aerospace Centre in 2002. It consisted of an electric powered controlled friction brake with self-reinforcement capability [4]. This self-reinforcing effect was achieved by means of brake linings equipped with a wedge on their backside, resting on an abutment. An electric motor applied the actuation force to the pads along the tangential direction (i.e., parallel to the disc surface). This configuration offered a notable advantage, as the auxiliary force derived from the self-reinforcement effect contributed to building up the normal clamping force. As a result, the electric actuator had to deliver only a minor portion of the total actuation force otherwise required in conventional electric braking systems without the self-reinforcement principle—systems that would otherwise demand large and heavy electric motors. eBrake® was the first electronic wedge brake (EWB) to be introduced, representing a specialized form of electromechanical brake (EMB) [5].

Over the years, many authors have investigated the modeling and control of EWBs. In [6], a mechanical dynamics model and a stability analysis of an EWB are presented. The model includes a description of the disc and pad friction characteristics, enabling investigation of the nonlinear behavior of self-energizing wedge brakes for different combinations of friction coefficient and wedge angle.

In [7], an EWB model is developed that includes the representation of its permanent magnet electric synchronous motor (PMSM), worm gear/wheel and power screw/nut transmission, caliper, wedge, and a sliding mode control algorithm. The performance of this system is verified both in simulation and experimentally using a prototype EWB tested on a bench setup.

In [8], an externally adjustable screw-driven EWB with two independently movable wedges is proposed. Its key feature is the ability to vary the contact points between the wedges and the rollers, which alters the effective wedge angle as a function of the wedge displacement under braking. The simulation of a hard braking event clearly highlights the reduced motor torque and energy demand of the externally adjustable EWB compared to conventional and semi-adjustable configurations.

In [9], a novel EWB is proposed, consisting of a screw-driven inner brake pad with a wedge, a fixed outer brake pad, a fixed caliper, and a hybrid stepper motor. An active disturbance rejection control (ADRC) algorithm is implemented to improve system response and stability. The performance of the proposed system is assessed by numerical simulation.

Comprehensive surveys on electromechanical braking systems, electronic wedge brakes, and their control strategies can be found in [5,10].

As an alternative to electric actuators in EWBs, the use of magnetorheological (MR) fluids in wedge brakes is also discussed in the literature. In [11], a self-energizing, self-powered automotive MR brake-by-wire system is designed, modeled, and tested. The proposed MR brake combines a T-shape, drum-type MR brake with a wedge mechanism. According to the authors, this configuration can deliver high braking torque while consuming less power than EWBs, as it harvests energy during braking through a generator that powers the MR brake.

Lastly, wedge brakes with conventional hydraulic actuation have also been investigated. In [12,13], a self-energizing hydraulic wedge disc brake for automotive applications is presented. The model features a single wedge block (equipped with a brake lining) mounted in the floating caliper housing on one side of the disc, and a flat brake pad on the opposite side. The wedge block is actuated by a hydraulic piston, which is aslant with respect to the disc, and rollers are arranged between the wedge and the caliper housing to reduce friction and prevent jamming. The effect of this model on deceleration and actuation power is evaluated against a conventional braking system by simulating a full vehicle model. The results highlight a significant improvement in braking efficiency [13]. In other words, it can be stated that for the same hydraulic actuation force, the wedge brake generates a higher braking torque, while for the same target torque, the wedge brake requires a lower hydraulic actuation force [12].

It is on this simple, yet effective principle that the wedge calipers object of this paper are based. In top-level motorsport world championships such as F1 and MotoGP, high-performance hydraulic disc brakes with fixed aluminum calipers are currently employed, coupled with carbon-carbon (C/C) discs and pads. Self-energizing wedge solutions have been introduced in recent years, primarily with the goal of reducing mass. In fact, a properly designed wedge-amplified braking system can achieve the same target braking torque as a standard caliper (i.e., $\alpha = 90°$, with reference to Figure 1) at the same hydraulic pressure, while requiring a smaller total piston area facing the brake fluid. This enables the use of either a lower number of pistons or smaller piston diameters, thus reducing the overall weight of the braking system.

No papers were found in the literature with a specific reference to self-energizing hydraulic braking systems in racing and their thermoelastic modeling.

After introducing the wedge amplification principle in braking systems, the goal of this paper is to revise and adapt the previously developed thermoelastic finite volume method (FVM) model—fully described and validated for a standard caliper in [14,15]—to extend its applicability to predict the braking performance of self-energizing high-performance C/C brakes, specifically with reference to the current braking systems used in F1. Therefore, the present work is conceived as a continuation of previous studies and directly addresses identified future developments.

To the authors' knowledge, this is the first work in the literature applying the reduced-order FVM approach—coupled with a local friction coefficient law—to the thermoelastic modeling of high-performance wedge-amplified C/C braking systems, in contrast to earlier automotive EWB/hydraulic wedge studies found in the literature. The key advantage of the proposed model is the reduced computational cost required to simulate a braking maneuver per unit time (about 20 min/s of simulation during braking on an Intel i7 processor–3 GHz, 24 GB RAM), compared to coupled thermoelastic finite element method (FEM) models of the braking system assembly (20 h/s of simulation, Intel i7 processor–3.6 GHz [16]). As such, the proposed model is intended to serve as a predictive tool to evaluate the mechanical and thermal performance of existing and new braking systems under different operating conditions, thanks to the possibility of simulating braking torque and temperature profiles over time for individually simulated braking maneuvers or full laps.

The paper is structured as follows. In Section 2 the amplified braking systems currently used on F1 cars are introduced and their main features are briefly described. The theoretical gain (also known as the global friction coefficient) is derived analytically for a generic wedge caliper layout with normal hydraulic actuation (i.e., piston forces applied perpendicularly to the disc surface) based on a simplified equilibrium analysis of the pad. The influence of various combinations of the wedge angle and disc-pad friction coefficient is pointed out. Then, the dynamometer used to perform experimental test cycles for the braking systems analyzed in this work is briefly described, along with a summary of the key features of the thermoelastic model developed in Dymola introduced in [14]. The model is revised by updating the definition of the boundary conditions of the pad in the exit region to correctly account for the self-energizing wedge effect. In Section 3 the updated model is validated mechanically and thermally—as extensively done in [15] for a standard front F1 caliper—considering several amplified calipers with different geometric features (i.e., wedge angles and number and size of pistons). Lastly, the thermoelastic model is used as a predictive tool to preliminarily assess the expected brake performance of a new caliper prototype that has not yet been manufactured and tested.

2. Materials and Methods

2.1. Self-Energizing High-Performance C/C Brakes

The key features of modern high-performance C/C brakes are briefly reviewed in this section, with a focus on modern F1 braking systems. According to the 2025 FIA F1 Technical Regulations, fixed aluminum hydraulic brake calipers must be used, with a modulus of elasticity not exceeding 80 GPa [17]. The maximum number of pistons per caliper is currently restricted to six. The discs are limited to a maximum thickness of 32 mm, with external diameters ranging from 325 mm and 330 mm at the front, and from 275 mm and 280 mm at the rear. No more than two pads per wheel are allowed, and cooling holes in the pads are prohibited [17]. Discs and pads are made of C/C, a composite material in which both the matrix and the reinforcing fibers are made out of carbon. The manufacturing process adopted by Brembo is chemical vapor infiltration (CVI), which provides the best results in terms of mechanical and thermal properties (summarized in Table 1) of the resulting composites [18].

The technical regulations do not prohibit the use of self-energizing braking mechanisms, provided that all other aforementioned technical requirements are met. Therefore, wedge-amplified solutions must share the same materials and components as standard systems. The only differences are in the geometry of the brake pads and the internal caliper surfaces that interface with them. A comparison between a standard and an amplified front braking system of a modern F1 car is illustrated in Figure 2.

Table 1. Main thermal and mechanical material properties of C/C composites in this study, adapted from [15].

Quantity	Unit	Value
Density	g/cm^3	1.8
Elastic modulus	GPa	10–20 ($r\theta$) 5–10 (z)
Specific heat	J/(kgK)	600
Thermal conductivity	W/(mK)	50–100
Thermal expansion coefficient	–	$<1 \times 10^{-6}$

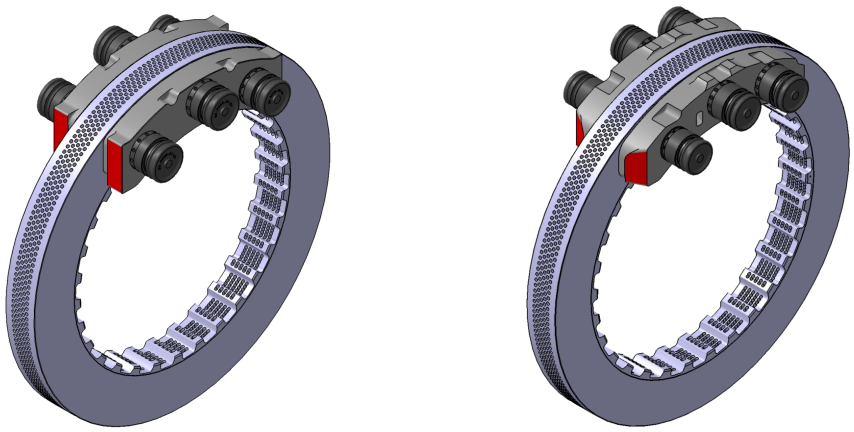

(**a**) (**b**)

Figure 2. Comparison between two modern F1 braking systems (pistons, pads, and disc are shown). The pad exit region is depicted in red and the disc rotates counter-clockwise. (**a**) Standard front braking system. (**b**) Amplified front braking system.

From the comparison, the distinct shape of the brake pads in the exit region can be clearly observed in the two configurations, highlighting an analogy between the wedge-amplified solution (Figure 2b) and the simplified schematic shown in Figure 1. During braking, the reaction forces that arise at the wedged interfaces between the caliper and the brake pads have a component perpendicular to the disc surface, which contributes to the total clamping force along with the hydraulic force applied by the pistons. This configuration complies with article 11.4.2 of the technical regulations [17], which states that "no braking system may be designed to increase the pressure in the brake calipers above that achieved by the driver applied force to the pedal under all conditions". This self-energizing principle thus allows for an increase in the total clamping normal force applied to the disc, without altering the hydraulic pressure generated by the driver's input. It is worth noting that, unlike self-energizing mechanisms commonly used in automotive applications, both brake pads in this solution are wedge-shaped and no rollers are used to reduce friction at the wedge-caliper interface. The amplified braking systems currently used in F1 can therefore be classified as friction brakes with fixed hydraulic wedge calipers. These systems are used by teams on the front axle, rear axle, or both.

2.1.1. Simplified Pad Equilibrium

The simplified equilibrium of the brake pad provides a basis for deriving a concise yet effective analytical expression for the expected gain of a given self-energizing caliper configuration. The corresponding schematic is shown in Figure 3, where a wedge-shaped pad is illustrated along with the main forces that act on it in the zx plane during braking. In this analysis, the wedge and the caliper are assumed to be rigid, and the inertial terms are neglected since stationary conditions are considered [3]. The friction force on the pad

support is neglected, and it is assumed that the friction force $F_{f,w}$ acting on the wedge surface does not have a component in the vertical direction y. $F_{z,pist}$ is the total hydraulic force applied by the pistons on the pad, $F_{z,disc}$ is the total clamping force exerted by a single pad on the disc, F_b is the braking force per pad, $F_{f,pist}$ is the total friction force between the pad and the pistons, and F_n is the reaction contact force between the pad and the caliper, normal to the wedge surface. In the scheme, μ, μ_p, and μ_w represent respectively the mean effective friction coefficient at the disc-pad interface, the friction coefficient between the pad and the pistons, and the friction coefficient between the pad and the caliper at the wedge interface.

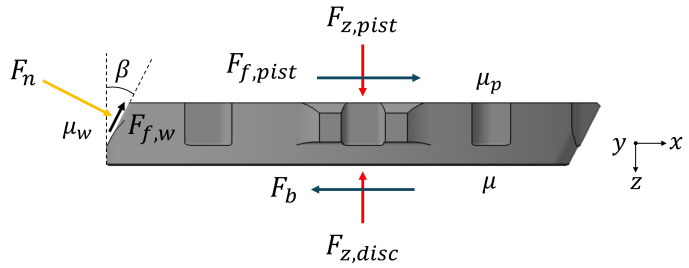

Figure 3. Simplified pad equilibrium under braking on zx plane.

Starting from the schematic in Figure 3 and applying the force equilibrium along the x and z directions, the system in Equation (1) holds.

$$\begin{cases} F_{z,pist} + F_n \sin\beta - F_{f,w}\cos\beta - F_{z,disc} = 0 \\ F_n \cos\beta + F_{f,pist} + F_{f,w}\sin\beta - F_b = 0 \\ F_b = \mu F_{z,disc} \\ F_{f,w} = \mu_w F_n \\ F_{f,pist} = \mu_p F_{z,pist} \end{cases} \tag{1}$$

From the second equation of the system, which expresses the equilibrium along the x direction, the reaction force F_n on the wedge can be derived according to Equation (2).

$$F_n = \frac{F_b - \mu_p F_{z,pist}}{\cos\beta + \mu_w \sin\beta} \tag{2}$$

By substituting the expression of F_n into the first equation of the system, the equilibrium along the axial direction z can be rewritten as shown in Equation (3).

$$F_{z,pist}\left(\mu\cos\beta + \mu\mu_w\sin\beta - \mu\mu_p\sin\beta + \mu\mu_w\mu_p\cos\beta\right) = F_b(\cos\beta + \mu_w\sin\beta - \mu\sin\beta + \mu\mu_w\cos\beta) \tag{3}$$

Based on the definition of gain coefficient μ_g as the ratio of the braking force F_b to the actuation force $F_{z,pist}$ (denoted as F_m in Figure 1), Equation (4) is obtained.

$$\mu_g = \frac{F_b}{F_{z,pist}} = \mu\frac{(\cos\beta + \mu_w\sin\beta - \mu_p\sin\beta + \mu_w\mu_p\cos\beta)}{(\cos\beta + \mu_w\sin\beta - \mu\sin\beta + \mu\mu_w\cos\beta)} \tag{4}$$

According to Equation (5), the gain coefficient can also be derived analytically from experimental data obtained during tests on a dynamometer, using the measured braking torque BT and hydraulic pressure p_{hydr}. Since the caliper geometry is known, that is, the total area of the pistons A_{pist} (per side, facing the brake fluid) and the effective radius R_{eff} of the caliper (defined as the weighted average of the radial coordinates of the centers of

the pistons, using as weights the areas of each piston), μ_g can be calculated directly from experimental input.

$$\mu_g = \frac{F_b}{F_{z,pist}} = \frac{BT}{2p_{hydr}A_{pist}R_{eff}} \tag{5}$$

Based on Equation (4), assuming $\mu_w = \mu_p \neq 0$ and positive, $\mu > \mu_w$, and $\beta \in [0, 90°]$, Equation (6) defines the wedge angle $\overline{\beta}$ such that μ_g becomes infinite.

$$\overline{\beta} = \arctan\left(\frac{1 + \mu\mu_w}{\mu - \mu_w}\right) \tag{6}$$

If $\beta < \overline{\beta}$, $\mu_g > 0$, the system is stable, and self-locking of the wedge does not occur. In contrast, if $\beta > \overline{\beta}$, $\mu_g < 0$, the actuation force becomes negative and the mechanism must be pulled. At the stability threshold $\beta = \overline{\beta}$, μ_g is infinite and the actuation force is theoretically null. In this condition, the braking maneuver is self-sustained and no external energy is needed [3,4].

By assuming zero friction at the interfaces between the pad and the caliper and between the pad and the pistons (i.e., $\mu_w = \mu_p = 0$), and by defining the wedge angle $\beta = 90° - \alpha$ (with reference to Figures 1 and 3), Equation (4) can be reformulated as Equation (7).

$$\mu_g = \mu\frac{\cos\beta}{\cos\beta - \mu\sin\beta} = \mu\frac{\sin\alpha}{\sin\alpha - \mu\cos\alpha} = \mu\frac{\tan\alpha}{\tan\alpha - \mu} \tag{7}$$

Accordingly, the stability threshold is expressed by Equation (8). In this case, stability is guaranteed for $\alpha > \overline{\alpha}$.

$$\overline{\alpha} = \arctan(\mu) \tag{8}$$

The same analytical expressions as in Equations (7) and (8) were derived in the literature [3] for the case of a rigid caliper and wedge brake actuation along the normal direction (i.e., perpendicular to the disc braking surface). Lastly, it is worth noting that, being $\beta = 90° - \alpha$, the imposition of $\mu_w = 0$ in Equation (6) leads to the result in Equation (8). In the next section, the nonlinear analytical expression of $\mu_g(\mu, \mu_w, \mu_p, \beta)$ is analyzed as a function of different combinations of the wedge angle β and the friction coefficient μ between the disc and the pad.

2.1.2. Gain Coefficient Dependencies

The analytical expression of μ_g, derived from the simplified pad equilibrium and reported in Equation (4), is plotted in Figures 4 and 5 as a function of the wedge angle $\beta \in [0, 40°]$ and the mean effective friction coefficient $\mu \in [0.2, 0.7]$ at the disc-pad interface. A single low reference value of $\mu_w = \mu_p \neq 0$ is assumed, consistent with the values adopted by designers and CAE engineers [14] during the design process of the calipers examined in this study.

It is worth noting that, for these values of wedge angles and friction coefficients, the resulting value of μ_g is always positive (as shown in Figures 4 and 5) and far from self-locking. In fact, also considering the highest value of friction coefficient analyzed in this section ($\mu = 0.7$), the evaluation of Equation (8) leads to a stability threshold $\overline{\alpha} = 35°$. This corresponds to an angle of 55°in terms of β, which is larger than the maximum wedge angle tested in this study ($\beta = 40°$). Note that Equation (8) is more conservative than Equation (6), as values of $\mu_w = \mu_p \neq 0$ increase the value of β at which instability occurs, for a given value of μ. Based on Equation (8), the instability threshold for a configuration with wedge angle $\beta = 40°$ occurs for $\mu \approx 1.2$, which is substantially higher than the friction coefficient values typical of braking system materials.

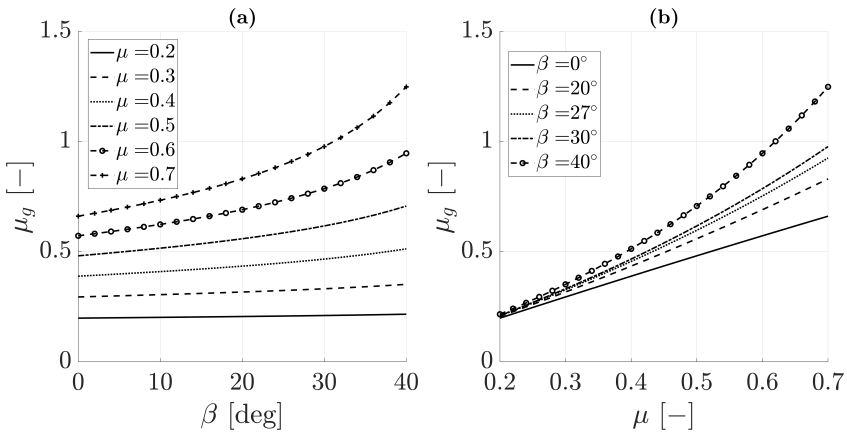

Figure 4. Gain coefficient μ_g of wedge amplified calipers as a function of (**a**) wedge angle β and (**b**) mean effective friction coefficient μ between the disc and pads, at a fixed value $\mu_w = \mu_p \neq 0$.

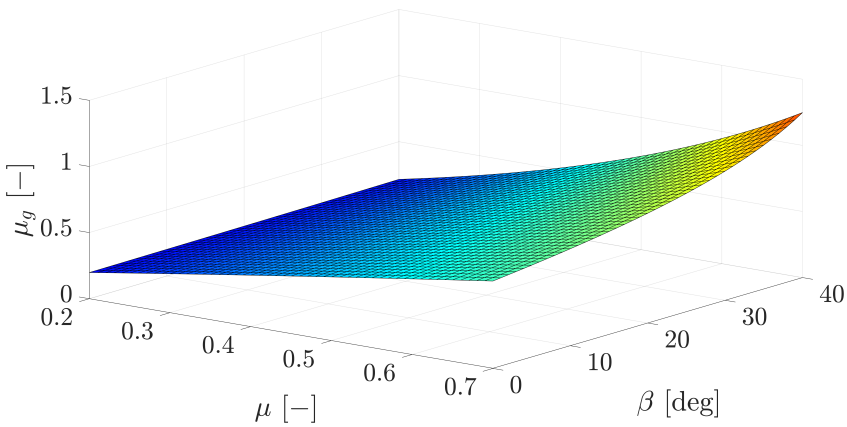

Figure 5. 3D representation of gain coefficient μ_g as a function of wedge angle β and disc-pad effective friction coefficient μ at fixed values of $\mu_w = \mu_p \neq 0$.

The expression reported in Equation (4), when combined with Equation (5), provides a valuable tool for the design and sizing of wedge-amplified brake calipers. Setting as a target the ability to generate the same braking torque BT at the same hydraulic pressure p_{hydr}, and assuming a fixed effective radius R_{eff}, the relationship in Equation (9) is derived.

$$\mu_{g,1} A_{pist,1} = \mu_{g,2} A_{pist,2} \tag{9}$$

As an example, assuming a reference friction coefficient of $\mu = 0.45$ and wedge angles $\beta_1 = 0°$ and $\beta_2 = 20°$, the corresponding gain coefficients yield a ratio of piston areas $A_{pist,2}/A_{pist,1} \simeq 0.878$. This corresponds to a 12% reduction in the total piston area for the amplified caliper, enabling a non-negligible weight saving through appropriate piston downsizing. This reduction in unsprung mass leads to improvements in the road holding index [1,19].

2.2. Experimental Setup

The braking systems in this study are experimentally tested using a full-scale dynamometer (TecSA TC 225 [20] in Figure 6), designed to replicate the working environment of high-performance brakes. The dynamometer is equipped with a torque sensor (error ±0.04% FS) for the measurement of braking torque, and the disc is driven by an electric motor that has a power of 450 kW and a maximum speed of 3500 rpm. Temperature acquisition involves the use of sunk thermocouples within brake pads, thermocouples to monitor caliper temperature, and pyrometers (Texense INF-T 1000-V2 [21] with accuracy 1% FS) to

measure disc surface temperature (nominally pointing at the mean radius of the braking band and diametrically opposite to the caliper). Effective thermal management is guaranteed by forced convection, providing to the braking system airflow controlled as a function of speed. The test bench runs dynamic cycles, categorized as either pressure-controlled (e.g., MAP, HD, HT) or torque-controlled (e.g., BAH).

All raw data are originally sampled at 1000 Hz, and are typically saved at the standard frequency of 200 Hz. Braking torque and hydraulic pressure signals are processed using a low-pass spatial filter instead of a traditional time-domain filter. This approach is necessary because a variable angular speed causes rotational frequencies (*1x*, *2x*, etc.) to shift in the time domain (Hz), whereas they remain constant in the spatial domain (m^{-1}). The cutoff frequency is set at $f_{cut} = 0.7/(2\pi R_w)$, slightly below the *1x* spatial frequency (where R_w is the wheel radius). Filtering is implemented in MATLAB R2024b using the *butter* and *filtfilt* functions. This configuration results in a zero-phase response with an effective fourth-order attenuation (due to the double-pass application of a second-order Butterworth filter). An in-depth description of the test bench and test cycles is provided in [15].

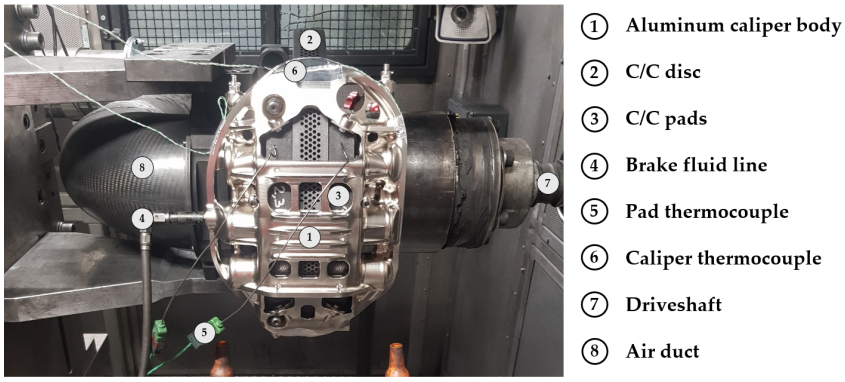

Figure 6. Experimental setup for the testing of a high-performance C/C braking system, adapted from [15].

2.3. Thermoelastic Modeling of Self-Energizing Brakes

2.3.1. Thermoelastic Model Overview

The thermoelastic model described in detail in [14] and mechanically and thermally validated extensively in [15] on a standard front F1 caliper is adapted for simulation of wedge-amplified braking systems. The key features of the proposed model are briefly summarized in this section. Interested readers are encouraged to consult previously published studies for the detailed derivation of the model.

The model is implemented in Dymola, a simulation environment based on the Modelica object-oriented modeling language [22–24], and it extends the framework originally developed by Kim et al. [25] to a 3D formulation, accounting for the orthotropic properties of C/C materials. The simplified geometries of the disc and pads (Figure 7b) are discretized using a FVM approach. To account for the complex geometry of the actual disc and pads, equivalent thermal and mechanical properties are computed and assigned to each finite volume element of the mesh in Dymola. A dedicated macro extracts from the CAD models of the actual disc and pads the values of volumes and areas of the different regions in which they have been partitioned [14]. Based on these values, solid to void ratios are computed and used to scale the mechanical and thermal properties of the materials. As an example, for a given element of the mesh in Dymola, its equivalent density is defined as the product of the material density of C/C and a solid to void volume ratio, defined as the ratio of the corresponding volume in the actual disc to the volume of the solid element of the Dymola

mesh. Both disc and pad models are based on the same architecture, consisting of elements, linkages, and boundary condition submodels (Figure 7a).

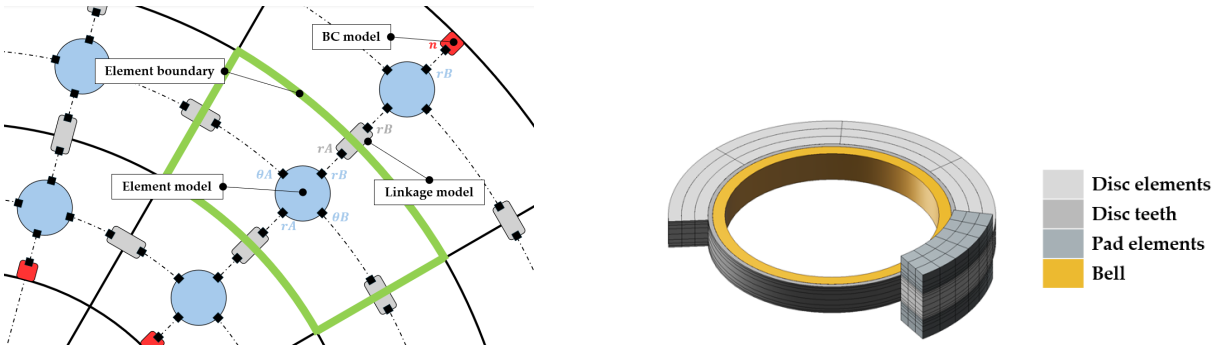

(**a**) (**b**)

Figure 7. Thermoelastic model overview, adapted from [15]: (**a**) 2D representation of the disc and pad models structure and their submodels. (**b**) Graphical representation of the FVM model mesh in Dymola.

Elements are submodels where energy balance and static mechanical equilibrium equations are enforced on the mass of a finite volume. The energy balance equation of an element takes into account the heat fluxes coming from the six connectors of the element (i.e., conduction between confining elements or boundary regions), the thermal power dissipated by convection (i.e., ventilation), and the storage term.

Linkages correspond to the interfaces that connect two elements along a certain direction (i.e., radial r, axial z, or tangential θ), modeling their thermal interactions using thermal resistances. The forces entering the mechanical equilibrium equation of an element are transmitted from linkage submodels, where they are computed starting from stress-strain relationships valid for orthotropic materials and accounting for the thermal expansion effect.

Lastly, boundary conditions are the submodels that link an element to an external boundary region, where loads, displacements, and thermal conditions are imposed or computed. The thermal and mechanical equations of every submodel are reported and commented on in [14]. In general, the boundary regions facing the ambient air exchange heat through convection and radiation. When convection is involved, it is modeled using heat transfer coefficients (derived from CFD simulations) that vary linearly with speed. Unlike the disc and pads, the pistons, the caliper, and the disc bell are modeled as concentrated masses that exchange heat with the surrounding components of the brake assembly and with ambient air.

The mechanical interaction between the pad and the caliper is modeled through a simplified strategy based on penalty contacts, imposed at user-defined locations on the pad through the definition of boolean matrices. Referring to the contact between the disc and the pads, a dedicated submodel computes the tangential friction force, the thermal power generated, and its repartition for each pair of disc and pad elements. The heat repartition model is based on the work of Lee et al. [26]. Based on this heat partition model, for both the disc and the pad, the thermal power entering one element accounts for two contributions. The first is computed on the basis of material properties, whereas the second accounts for conduction between the two elements in contact.

The local friction law implemented in the model is a static, analytical, and semi-empirical friction formulation that takes as input the local contact pressure, temperature, and sliding speed and computes the local friction coefficient for each pair of disc and pad elements in contact. The same friction model defined in [14,15] applies in the present work.

Based on the observation of experimental dyno data, two friction phases are distinguished: the initial friction build-up phase (i.e., lasting 0.1–0.15 s since the start of braking) and the pressure modulation (and release) phase. For both mentioned phases, an analytical formulation of the type given in Equation (10) is adopted, while the transition between the phases is modeled using a sigmoid-type function. Figure 8 presents the local friction coefficient μ_l as a function of local variables during pressure modulation. The key feature of the law is the (nonlinear) reduction in local friction μ_l as the contact pressure p_l increases.

$$\mu_l = \mu_l(p_l, T_l, v_l) = \sum_{i=1}^{n} d_i f_i(p_l, T_l, v_l) \tag{10}$$

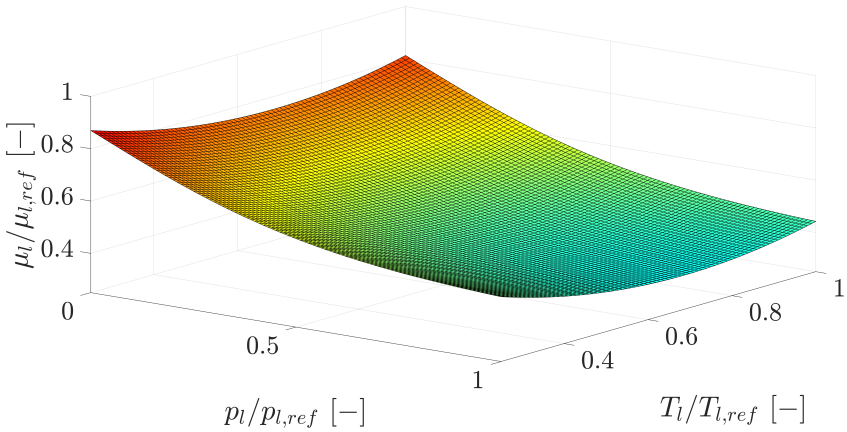

Figure 8. 3D representation of the local friction law as function of contact pressure and temperature at fixed sliding speed, adapted from [15].

The three variables p_l, T_l, and v_l are calculated in the contact submodel of each pair of disc and pad elements. Local contact pressure p_l is defined as the ratio of the axial force acting on the element (derived from the solution of the mechanical equilibrium equation of the element) to its axial surface area. Local temperature T_l is the temperature of the corresponding first disc element along the axial direction (derived from the solution of the thermal balance equation of the element). Lastly, the local sliding speed v_l is calculated as the product of the disc angular speed ω and the radial coordinate of the element considered. The numerical procedure used to derive the coefficients d_i is detailed in [15].

2.3.2. Model Extension to Wedge Calipers

To adapt the Dymola thermoelastic model to wedge amplified calipers, a relevant modification is implemented in the baseline version of the model. The adjustment concerns the modeling of the tangential loaded boundary region of the pad—corresponding to its exit side (marked in red in Figure 2)—where the reaction forces that balance the braking torque arise. In the finite volume model of the pad, three different surface conditions are distinguished within this boundary region [14].

- Support contact zone, which provides a normal reaction force (i.e., along the y direction in Figure 3) that prevents pad motion toward the internal radius. In this work, the modeling of this zone remains unchanged.
- Tangential contact zone, which provides the normal reaction contact force with the caliper. This is the zone where the distinction between a standard caliper (i.e., $\alpha = 90°$) and a wedge caliper (i.e., $\alpha < 90°$) must be introduced.
- Unloaded zone.

The distinction between the three cases is determined by the user through two distinct boolean matrices, which define the elements belonging to the wedge and those belonging

to the support. The same considerations described in [14] generally apply also to the FVM models of wedge-amplified calipers: penalty contacts for the tangential contact zone are assigned to the elements having the highest radial coordinate, as it is the region most heavily loaded on the wedge surface, and it is assumed that the direction of friction forces on the wedge surface is inclined at 45°. These modeling assumptions are based on the observation of available FEA results from current and past braking systems. As an example, the contact normal stress (CNS) and friction force distributions computed on the wedge surface of caliper C (see Table 2 in Section 3.1) are shown in Figure 9. Details on the structural FEA methodology used are found in [14].

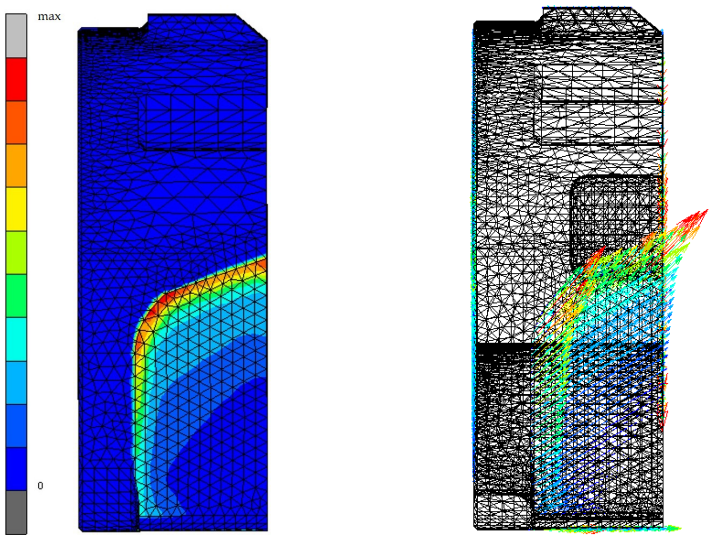

(**a**) (**b**)

Figure 9. Example of FEA for a wedge-amplified braking system (caliper C): (**a**) CNS distribution on the wedge surface. (**b**) Friction forces (direction and magnitude) on the wedge surface.

Table 2. Main geometric data of the C/C braking systems analyzed.

Caliper	β [°]	A_{pad} [mm^2]	A_{pist} [mm^2]	R_{eff} [mm]	d_e [mm]	t_d [mm]	t_p [mm]
A	0	7771	2620	143	328	32	22
B	20	7643	2315	141	328	32	22
C	27	6769	2315	145.5	330	32	23.5
D	40	6412	2315	145.5	330	32	23.5
X	40	7184	2036	143	328	32	22

With reference to Figure 10, for a generic wedge-amplified caliper, the system in Equation (11) holds.

$$\begin{cases} u_s = (side)u_{\theta,BC}\cos\gamma + u_{r,BC}\sin\gamma \\ u_n = u_s\sin\alpha + u_{z,BC}\cos\alpha \\ F_n = k_{BC}u_n \\ F_{f,a} = F_{f,v} = \frac{1}{\sqrt{2}}\mu_w F_n \\ F_{f,a} = F_{z,BC}\sin\alpha + F_s\cos\alpha \\ F_n = -F_{z,BC}\cos\alpha + F_s\sin\alpha \\ F_s = -F_{r,BC}\sin\gamma - (side)F_{\theta,BC}\cos\gamma \\ F_{f,v} = F_{r,BC}\cos\gamma - (side)F_{\theta,BC}\sin\gamma \end{cases} \tag{11}$$

In Equation (11), α and γ are, respectively, the wedge angle of the pad and the tangential coordinate of the boundary surface with reference to the mesh of the FVM model (i.e., $\gamma = \varphi/2$, where φ is the angular amplitude of the pad). The parameter k_{BC} is the stiffness of the penalty contact and μ_w is the friction coefficient between the pad and the caliper on the wedge surface. As introduced in [14], the parameter *side* is equal to ± 1 (i.e., $+1$ for the *top* pad and -1 for the *bottom* pad). The signs of forces and displacements in the r, θ, z directions are consistent with the local reference system of the pad (Figure 11), while along the n and s directions they are positive as contact occurs.

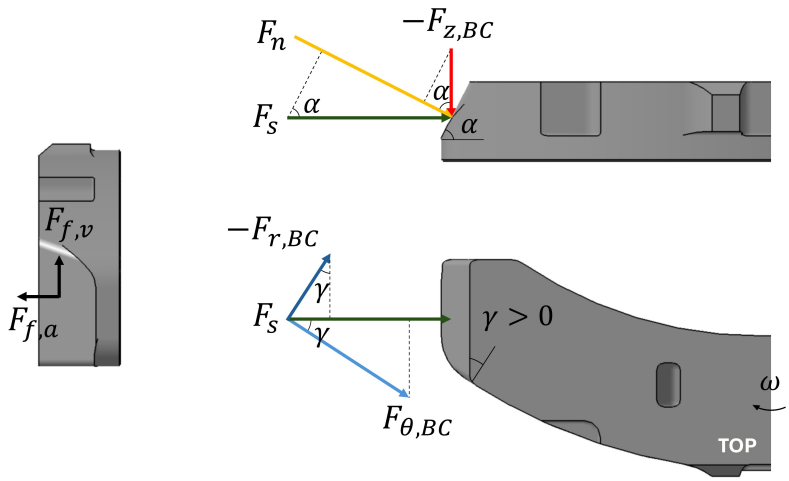

Figure 10. FVM model forces for the pad tangential loaded boundary region, adapted from [14].

It is worth noting that if $\alpha = 90°$, $u_s = u_n$, $F_s = F_n$, and the system in Equation (11) coincides with the equations reported in reference [14] for the modelling of non-amplified calipers.

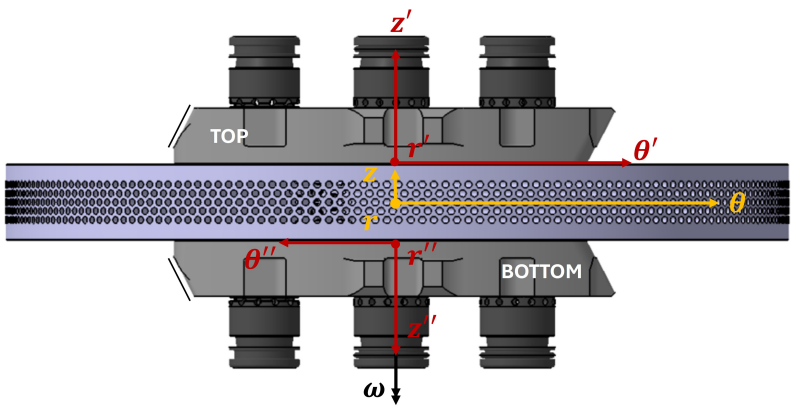

Figure 11. Disc (yellow) and pads (red) cylindrical and right handed reference systems, adapted from [14].

3. Results and Discussion

3.1. Model Validation on Wedge-Amplified Calipers

In this section, the adapted thermoelastic model is validated mechanically and thermally for different amplified calipers and test cycles, as done for a standard front F1 caliper (hereafter referred to as caliper A) in [15]. Each modeled amplified braking system has been used or prototyped between the 2022 and 2025 F1 seasons. The main features are summarized in Table 2 (together with those of caliper A for reference), where β is the wedge angle (with reference to Figure 3), A_{pad} is the pad area in contact with the disc, A_{pist} is the total area of the pistons facing the brake fluid (per side of the caliper), R_{eff} is the effective

radius, and d_e, t_d, t_p are respectively the external disc diameter, the disc thickness, and the pad thickness. The CAD model of each caliper body is shown in Figure 12, where the pad supports with different wedge angles are highlighted for each configuration. As mentioned in Section 2.3.1, mechanical modeling of the caliper body is not included in the proposed thermoelastic model. As a result, symmetric contact pressure distributions are simulated on the two sides of the disc.

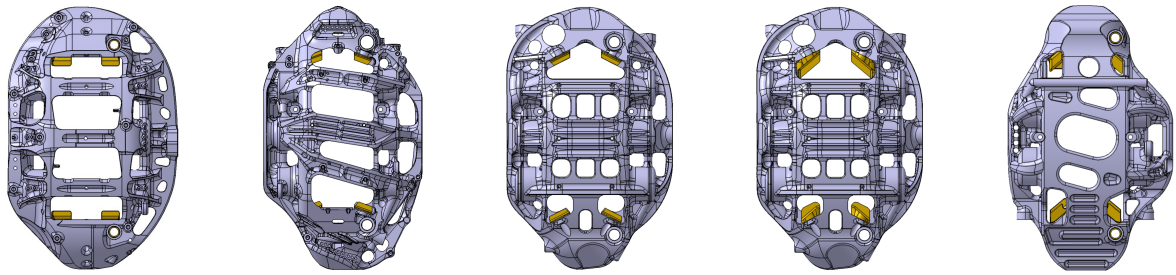

(**a**) (**b**) (**c**) (**d**) (**e**)

Figure 12. CAD models of the calipers and their pad supports for configurations: (**a**) Caliper A. (**b**) Caliper B. (**c**) Caliper C. (**d**) Caliper D. (**e**) Caliper X.

For each braking system, the same mesh already adopted and validated in [14,15] is used (see Table 3 and Figure 7b). Mesh refinements are applied along the circumferential direction in the contact region between the disc and the pads to better capture the resulting contact pressure distribution. Being circumferential temperature gradients small compared to those along the radial and axial directions, circumferential mesh refinements are not applied in the uncovered region of the disc. To capture the high temperature gradients along the disc and pad thickness, mesh refinements are necessary along the axial direction as well. A fixed axial discretization step (i.e., the ratio between the thicknesses of two consecutive elements along the axial direction) equal to 1.5 is set for both the disc and the pad elements. In this way, the distance from the center of the first element to the interface between the disc and the pad is below 1 mm. This setup features approximately 2×10^5 equations and unknowns.

For each simulation performed, the inputs provided to the model include the filtered hydraulic pressure or braking torque time history, the disc angular speed time history (unless it is computed as in Section 3.2), the initial temperatures of the disc, pad, and caliper, the coefficients defining the relationship between air flow rate and speed, the braking system geometry (including the specific dimensions and position of each piston, as well as the boolean matrices defining the locations of penalty contacts between the pad and the caliper), the solid to void volume ratios (SVVR) and solid to void surface ratios (SVSR) [14], the mechanical and thermal properties of the C/C materials, and the heat transfer coefficients (HTCs) of the disc regions and pads (from CFD).

Table 3. FVM model mesh.

Description	Symbol	Disc	Pad
No. of elements along r	N_r	3	3
No. of elements along θ	N_θ	15	9
No. of elements along z	N_z	8	5

As the scope of the model is to provide a mechanical and thermal performance assessment of a braking system, the main simulation outputs of interest are twofold.

- Braking torque or hydraulic pressure, depending on the type of model version used (i.e., if hydraulic pressure is provided as the input braking torque is the output, and vice versa).
- Disc surface temperature, evaluated in the diametrically opposite zone relative to the contact region and in the mean radius of the braking band along the radial direction, where pyrometers are typically placed during bench tests. The simulated surface temperature T_{sim} is defined through a linear extrapolation in Equation (12), using the temperatures of the two outermost mesh elements along the axial direction.

$$T_{sim} = T_{el,1} + \frac{T_{el,1} - T_{el,2}}{L_{z12}} \frac{\Delta z_1}{2} \tag{12}$$

$T_{el,1}$ and $T_{el,2}$ are the temperatures of the two elements, L_{z12} is the axial distance between their centers, and Δz_1 is the thickness of the outermost element. The radial and circumferential coordinates of these elements correspond to the location where the pyrometers are positioned.

For each braking system under analysis, the test bench setup introduced in Section 2.2 is used, and the same classes of test cycles described in [15] are performed. The following sections report the main simulation results obtained for each braking system in order to assess the accuracy of the proposed model. Both simulated and experimental results have been normalized with respect to reference values due to confidentiality. For a given variable, the same value is always used to normalize both simulated and experimental results, to ensure consistent comparisons among the different figures in this section.

3.1.1. Validation of Caliper B

Caliper B is an amplified front caliper used during the 2022 F1 World Championship, designed with six pistons (i.e., three per side) and a 20° wedge angle (Figure 12b). Figure 13 compares the contact pressure distributions on the pad (disc-side) between the thermoelastic FVM model and a static structural FEM model of the same braking system. The FEM model is defined according to the same methodology described in [14], without accounting for caliper compliance (i.e., replacing the caliper with rigid surfaces in contact with the pad and imposing displacement constraints for pistons). The local friction coefficient (imposed in this case uniformly distributed on the entire contact surface), the applied hydraulic pressure on the pistons, and the friction coefficient on the contact surfaces between the pads and the caliper are the same in both models. Qualitatively, good consistency is achieved, as the FVM model effectively detects and replicates the high contact pressure in the wedge region (i.e., the upper exit side of the pad). At the same time, the two low-pressure regions located between the pistons are also well captured, along with the medium-pressure region near the pad inlet side.

Table 4 compares the normalized reaction forces obtained in the different contact regions of the pad with respect to the FEM results, using the cartesian reference frame defined in Figure 3. Robust agreement is observed for the reaction forces along the horizontal (x, positive towards the inlet) and axial (z, positive towards the disc) directions. Conversely, the vertical direction (y, positive upward) exhibits the most significant variations between the models. These dissimilarities can be attributed to the distinct approaches utilized to model frictional effects in the two simulations. Specifically, the Dymola model imposes predefined directions for friction forces both in the wedge region and on the contact surface between the pad and the pistons. In contrast, the FEM simulation allows these friction directions to vary unconstrained. This results in an unloading of the caliper bridge in this FEM analysis, where the vertical load sustained by the support is counterbalanced by negative vertical reaction forces on both the disc-side and piston-side surfaces of the

pad. Table 5 (Section 3.1.2) presents the same analysis run for caliper C. The FEA predicts a significant loading condition on the bridge, and fairly aligned results between the FVM and FEM approaches are obtained along all three directions. As the friction parameters at the pad-caliper and pad-piston interfaces have not been experimentally validated, the accuracy of the FEM model in this aspect cannot be guaranteed. Therefore, the observed differences between the two models for caliper B are not considered a critical issue, and the accuracy achieved in the wedge region is deemed satisfactory for the intended application of the thermoelastic model.

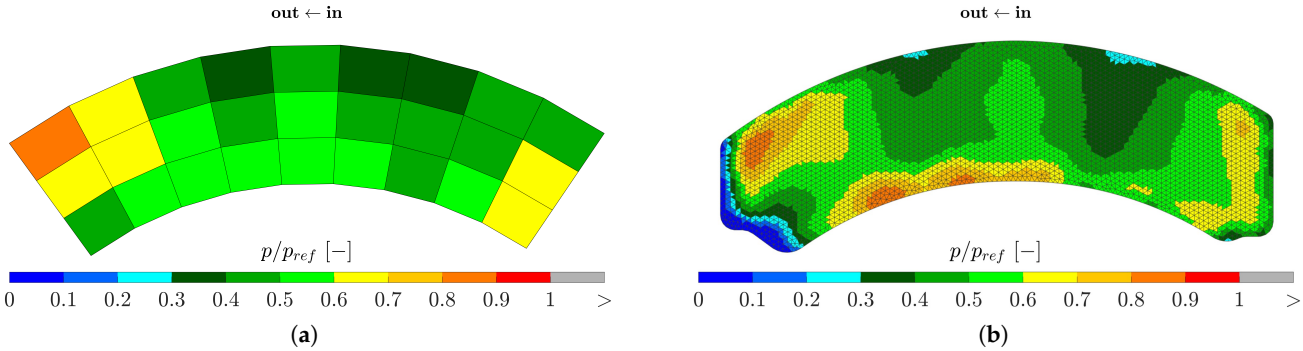

Figure 13. Normalized contact pressure distribution of caliper B (20°): (**a**) FVM Dymola model. (**b**) FEM structural model.

Table 4. Normalized reaction forces of caliper B (20°).

Boundary Zone	FVM			FEM		
	x	y	z	x	y	z
Disc-side	−0.422	−0.012	−1.000	−0.391	−0.037	−1.000
Piston-side	0.085	0.001	0.906	0.074	−0.065	0.916
Wedge	0.328	0.024	0.094	0.310	0.026	0.091
Support	0.008	0.082	0.000	0.002	0.065	−0.006
Bridge	0.000	−0.096	0.000	0.000	0.000	0.000
Total	−0.001	−0.001	0.000	−0.005	−0.011	0.001

Table 5. Normalized reaction forces of caliper C (27°).

Boundary Zone	FVM			FEM		
	x	y	z	x	y	z
Disc-side	−0.425	−0.016	−1.000	−0.423	−0.019	−1.000
Piston-side	0.082	0.001	0.858	0.096	−0.013	0.867
Wedge	0.336	0.026	0.142	0.327	0.024	0.139
Support	0.007	0.069	0.000	0.006	0.093	−0.003
Bridge	0.000	−0.079	0.000	0.008	−0.079	−0.002
Total	0.000	0.001	0.000	0.014	0.006	0.001

The model of caliper B is used to simulate a subset of the braking cycles performed on the dynamic test bench during the validation procedure of a caliper. Figures 14 and 15 show comparisons between simulated and experimental global friction maps under steady pressure conditions, as a function of the mean disc temperature and the synthetic index $p_c\omega$, where ω is the angular speed of the disc and p_c is the mean contact pressure. The lat-

ter is computed from the simplified pad equilibrium without accounting for the wedge contribution, as described in Equation (13).

$$p_c = p_{hydr} \frac{A_{pist}}{A_{pad}} \tag{13}$$

The simulated disc temperature is calculated according to Equation (12), while the gain coefficient is derived based on the braking torque, hydraulic pressure, and caliper geometry, as defined in Equation (5). For caliper B, two complete mapping cycles are simulated, each consisting of 128 braking events at four different target pressure levels, four speed intervals, and eight different initial temperatures. Overall, the simulations show favorable agreement with the test bench results, particularly across the mid-to-low temperature range. For reference, Figure 16 reports the same comparison for caliper A. As theoretically expected, caliper B yields higher values of the gain coefficient, as the denominator in Equation (5) does not account for the axial force contribution provided by the wedge.

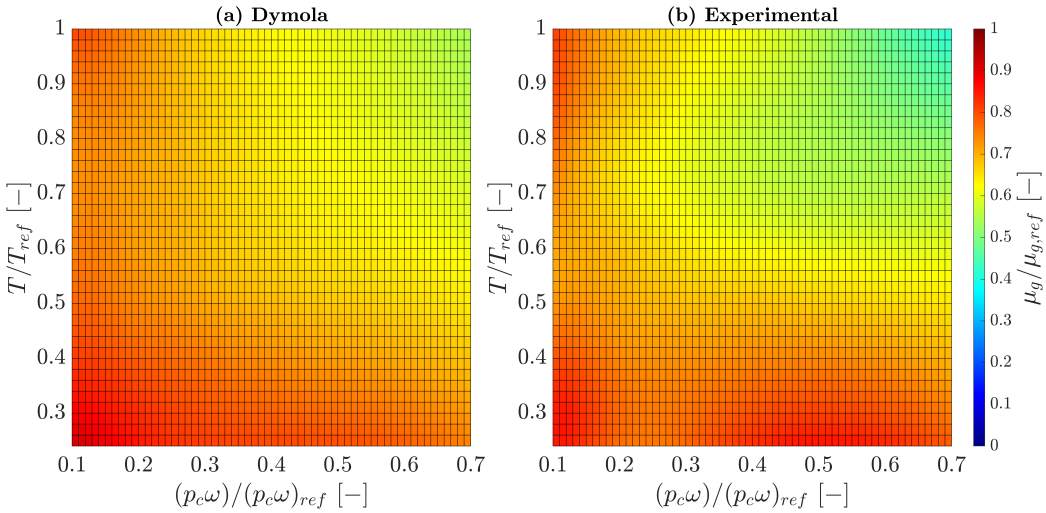

Figure 14. Comparison between (**a**) simulated and (**b**) experimental global friction maps of caliper B (20°)—first mapping cycle.

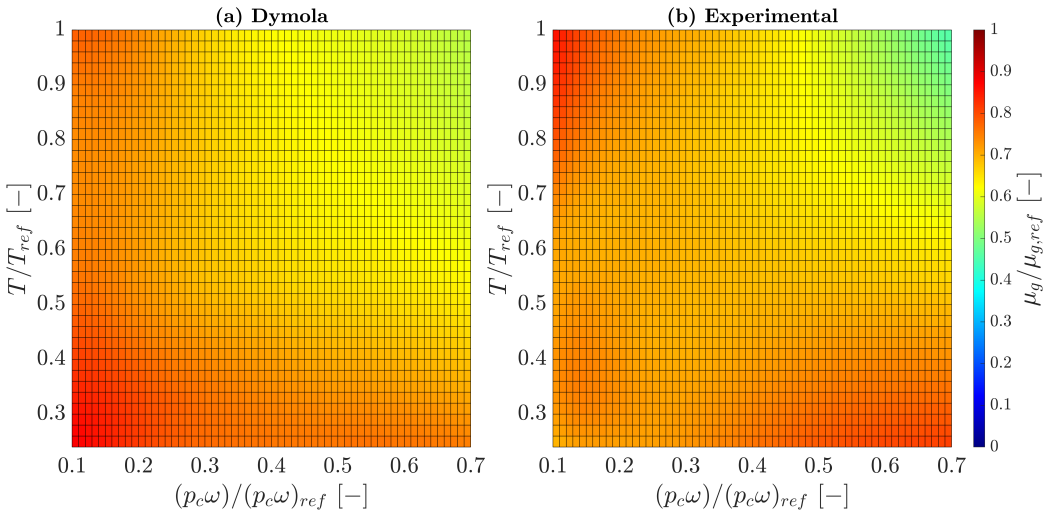

Figure 15. Comparison between (**a**) simulated and (**b**) experimental global friction maps of caliper B (20°)—second mapping cycle.

As discussed in [15], the experimental global friction maps of a given braking system are not unique; rather, they may exhibit variability due to differences in the performance characteristics of the specific set of disc and pads used during the testing. These variations—such as differences in the disc out-of-plane thermal conductivity (PP8 index [18]) and the amount of abrasive particles in the pads (PP4 index)—can be observed when comparing Figures 14b and 15b. Such dissimilarities in friction performance are detected during the bedding process, such that only disc and pad sets with comparable frictional behavior are paired on the same axle of the actual car.

The last results presented for caliper B refer to Bahrain cycles, which represent the reference telemetry cycles (torque and speed-controlled on the dyno [15]) performed during the experimental validation of the braking system. Figures 17 and 18 show, respectively, the simulations of two complete laps at different initial disc temperatures T_0 (i.e., low and high). In both cases, the experimental time histories of hydraulic pressure and rotational speed are provided as input to the model. The experimental disc temperature is defined as the average of the values measured by two pyrometers positioned on opposite sides of the disc (i.e., inboard and outboard) as described in Section 2.2.

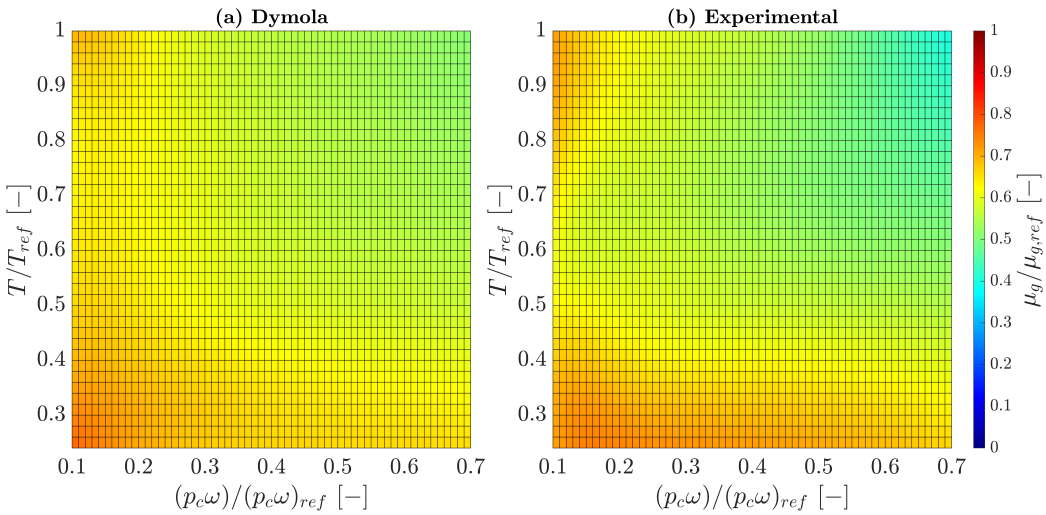

Figure 16. Comparison between (**a**) simulated and (**b**) experimental global friction maps of caliper A (standard), adapted from [15].

Model predictions for both braking torque and disc surface temperature show strong agreement with experimental observations. Taking as a reference the first and most demanding braking maneuver of the lap—corresponding to Turn 1—it is worth noting that achieving the same experimental peak torque at a higher initial temperature requires a 15% increase in the maximum input pressure due to the reduction in friction.

This dependence of friction on temperature—ascribable by Kasem et al. [27] to attenuation by oxidation of abrasive mechanisms as the temperature increases—is accurately captured by the FVM model and its local, analytical, and semi-empirical friction law. This finding is consistent with prior observations from Bahrain cycles performed and simulated with caliper A [15] (e.g., a 6% increase in maximum pressure was observed for the same analysis reported above for caliper B).

Although caliper A features a product $A_{pist}R_{eff}$ that is approximately 15% larger than that of caliper B, the latter—thanks to its 20° wedge angle—requires comparable values of hydraulic pressure (and therefore driver effort) to deliver the same target braking torque. Concurrently, caliper B offers a significant weight advantage, with a reduction of 17%. This performance trend is observed in both the experimental and simulated

mapping and telemetry cycles analyzed in this section for caliper B and in [15] for the non-amplified caliper.

The mean error indices for the simulation results of caliper B are summarized in Table 6, where they are calculated using the same formulations adopted in [15]. With reference to braking torque, for an individual braking maneuver indexed by j and its corresponding t time instants, the error indices are calculated according to Equations (14)–(17). The same set of equations is also applied to evaluate the error indices for the surface temperature of the disc.

$$EC_{rmse,j} = \sqrt{\frac{1}{t}\sum_{i=1}^{t}\left|BT_{exp,i} - BT_{sim_i}\right|^2} \tag{14}$$

$$EC_{nrmse_j} = \frac{EC_{rmse,j}}{\max(BT_{exp}) - \min(BT_{exp})} = \frac{EC_{rmse,j}}{\max(BT_{exp})} \tag{15}$$

$$EC_{peak,j} = \left|\max(BT_{sim} - \max(BT_{exp})\right| \tag{16}$$

$$EC_{npeak,j} = \frac{EC_{peak,j}}{\max(BT_{exp})} \tag{17}$$

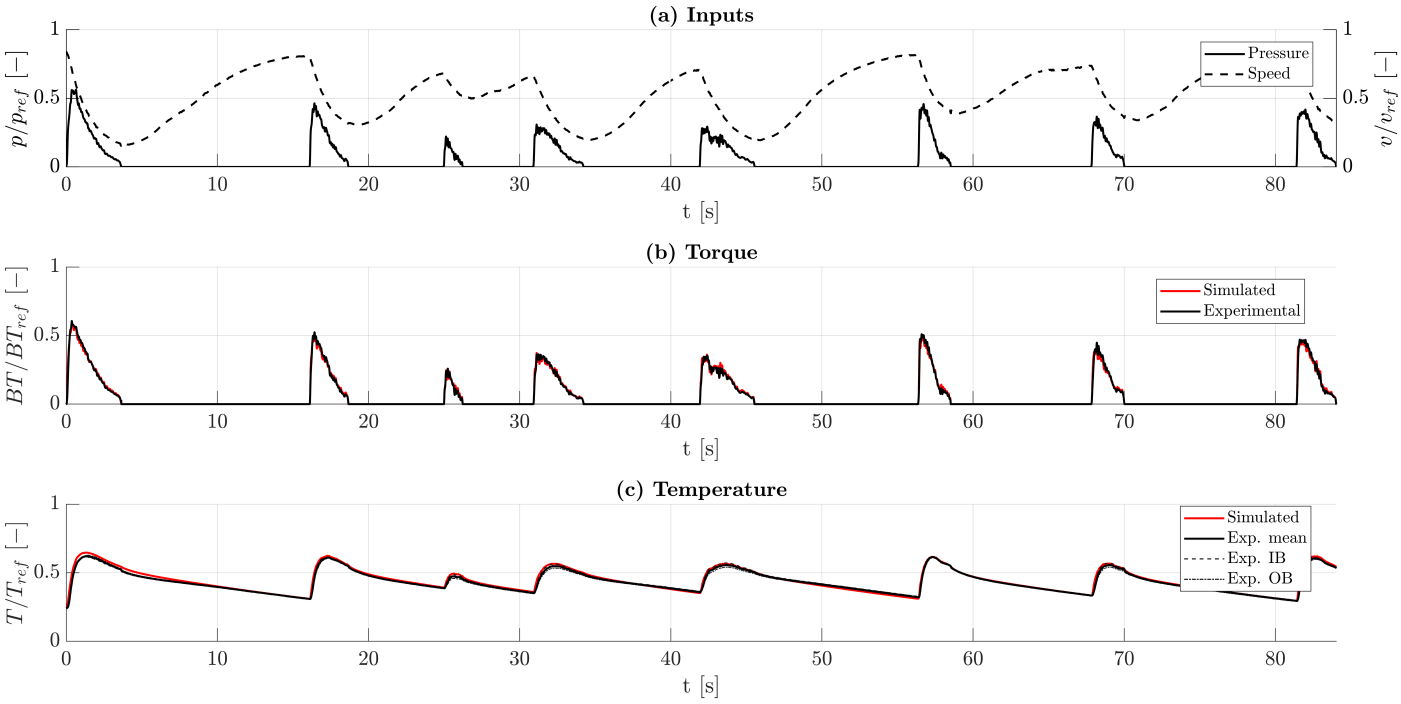

Figure 17. Bahrain cycle full lap simulation of caliper B (20°)—pressure and speed inputs—low starting temperature cycle.

The indices for the entire cycle are then calculated as the average of the corresponding indices for all N braking maneuvers simulated singularly. Overall, the simulation results demonstrate favorable agreement with the experimental data, with rmse for the temperature consistently below 50 °C and normalized peak torque errors below 5% for the majority of the simulated cycles. These results are particularly significant for the intended objectives of the model, as 20° wedge angles represent a design solution commonly adopted by teams for front calipers.

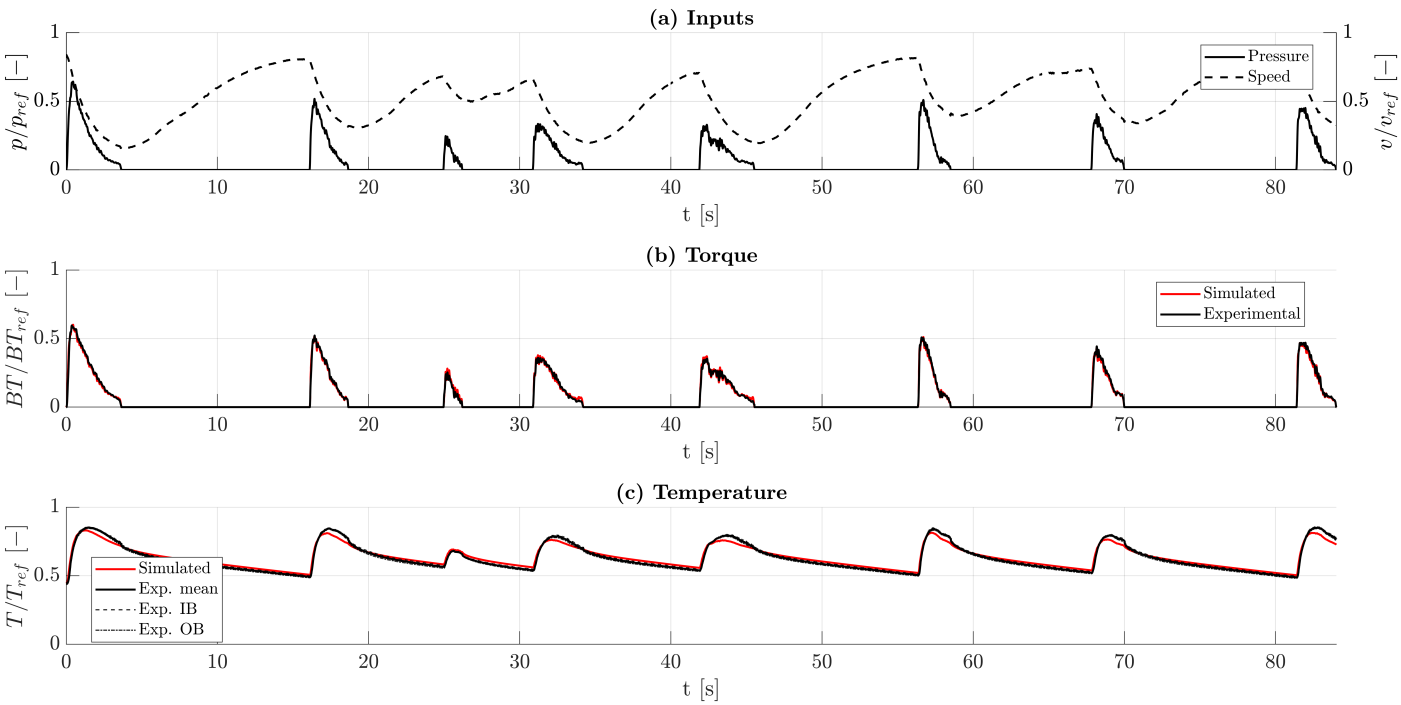

Figure 18. Bahrain cycle full lap simulation of caliper B (20°)—pressure and speed inputs—high starting temperature cycle.

Table 6. Mean error indices of the test cycles simulated for caliper B (20°)—braking maneuvers simulated individually.

Cycle	Notes	N	Mean Error Indices							
			ET_{rmse} [°C]	ET_{nrmse} [%]	ET_{peak} [°C]	ET_{npeak} [%]	EC_{rmse} [N m]	EC_{nrmse} [%]	EC_{peak} [N m]	EC_{npeak} [%]
MAP	-	128	25.6	9.5	25.4	4.0	181.5	7.3	124.0	4.7
MAP	-	128	24.3	8.7	27.1	3.8	238.3	9.0	247.0	8.2
BAH	Low T_0	16	27.5	13.3	19.5	3.5	139.5	5.5	110.1	4.5
BAH	Mid T_0	8	33.2	11.6	36.4	5.0	144.7	5.7	103.6	4.2
BAH	High T_0	8	34.5	11.4	37.7	4.6	96.9	4.0	61.7	3.2

3.1.2. Validation of Caliper C

Caliper C is a front F1 caliper prototype, compliant with current technical regulations, although it has not been used on track. It features a hydraulic layout with six pistons and a wedge angle of 27°. The total piston area is identical to that of caliper B, but it is combined with a larger wedge angle and a larger effective radius. Assuming a friction coefficient $\mu = 0.45$ and the same target braking torque, Equations (4) and (5), along with geometric parameters, indicate that caliper C theoretically requires a hydraulic pressure approximately 8.5% lower than caliper B and 7.8% lower than caliper A. The caliper is designed to accommodate different types of pad supports, each machined with varying wedge angle. The configuration shown in Figure 12c, with $\beta = 27°$, is analyzed in this section, while the configuration with $\beta = 40°$ will be addressed as caliper D in Section 3.1.3.

The simulation of a Bahrain cycle lap for caliper C at high starting temperature T_0 is shown in Figure 19. Satisfactory estimates of braking torque and disc surface temperature are achieved, further confirming the predicting capabilities of the proposed thermoelastic model. Focusing on the first braking phase, the high T_0 cycle exhibits a peak hydraulic pressure approximately 12% higher than that observed experimentally in the low temperature scenario, due to the temperature-induced reduction in friction. This trend, consistently ob-

served across all laps of the experimental cycles, is successfully captured by the model and aligns with the experimental and numerical findings of the Bahrain cycles of caliper A [15] and caliper B (Section 3.1.1). Furthermore, with reference to high temperature Bahrain cycles, caliper C shows experimental peak pressure values for each braking maneuver up to 7% lower than caliper B, thus confirming its higher efficiency.

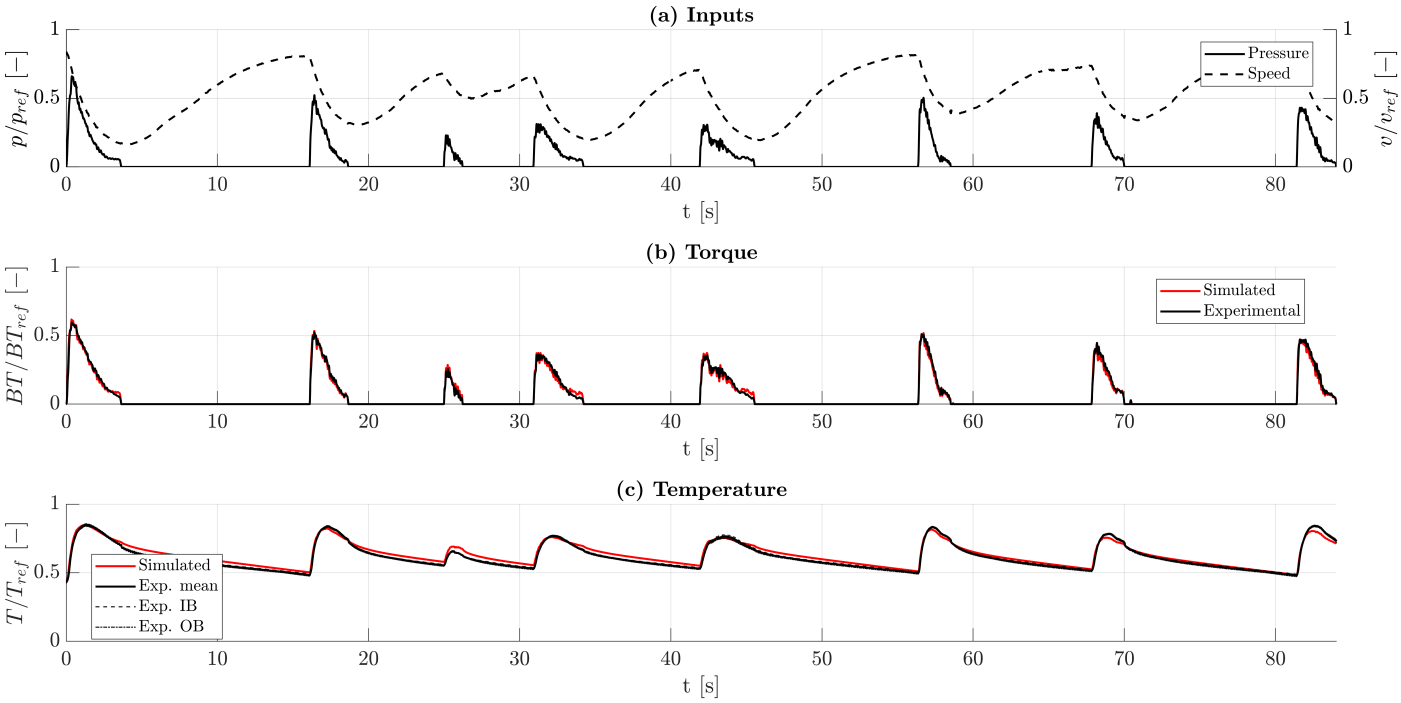

Figure 19. Bahrain cycle full lap simulation of caliper C (27°)—pressure and speed inputs—high starting temperature cycle.

A noteworthy observation arises from the high T_0 full lap simulation in Figure 19. Specifically, during the fourth and fifth braking events—characterized by similar torque and temperature levels—a sudden drop in the gain coefficient is observed, halving in the final second of pressure application. Under these conditions, the friction law of the model significantly overestimates the resulting braking torque, as it predicts an increasing trend of friction during the pressure release phase. For comparison, a single braking maneuver from a mapping cycle is shown in Figure 20.

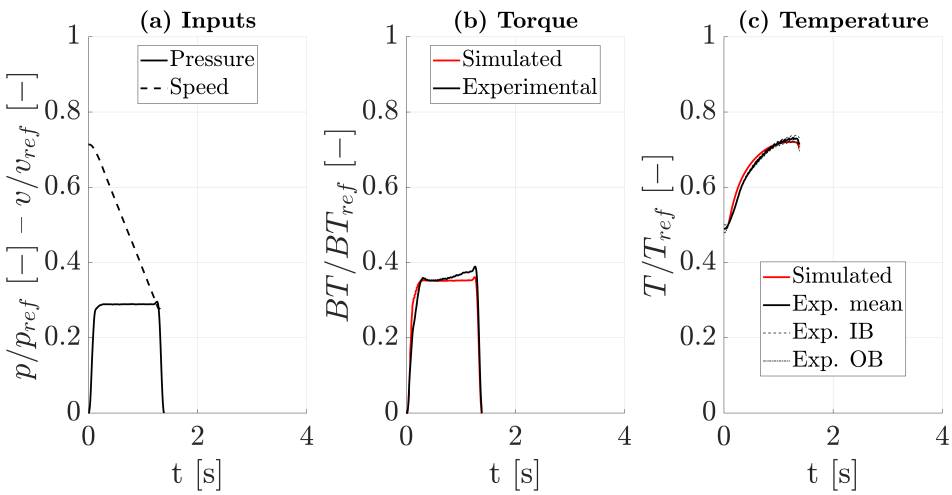

Figure 20. Simulation of an individual braking maneuver from a mapping cycle of caliper C (27°).

Although its initial temperature, initial speed, and pressure are similar to the aforementioned cases, the experimental data in this case do not exhibit the same friction drop. Friction is observed to increase throughout the braking event (i.e., torque increases at constant hydraulic pressure), causing the model to underestimate the braking torque by approximately 7% immediately preceding pressure release (Figure 20b). These experimental results—as also discussed for caliper A [15]—may suggest a possible dependence of experimental friction behavior on the time histories of preceding braking events within the specific cycle, as they can impact on the rate of generation, destruction, and regeneration of friction films that affect the tribological properties of C/C composites [28–30]. Capturing such complex friction dynamics is currently beyond the scope of the present model, which is intended to provide performance predictions of different braking system layouts based on a static analytical local friction formulation.

The last case discussed for caliper C considers a braking maneuver from a high torque cycle at the maximum applied pressure level, reaching a peak torque approximately 54% higher than those recorded during Bahrain cycles. This scenario involves the highest braking torque exerted by the braking system during its testing. The experimental results are shown in Figure 21, and are consistent with observations of high torque cycles of caliper A [15].

- A friction peak—known as bite—is observed after 0.1 s from the start of braking. The literature on C/C composites for aircraft brakes attributes this observed behavior to the desorption of adsorbed water vapor from the friction surface as the temperature increases [28,30,31].
- After the peak, friction decreases significantly to a minimum value (owing to the combined effects of local contact pressures and temperatures) and then increases again as the decrease in hydraulic pressure becomes the dominant factor. In Figure 21b, the experimental gain coefficient μ_g is calculated according to Equation (5), and the effective friction coefficient μ is estimated by solving the nonlinear Equation (4).
- As observed for caliper A [15], the minimum friction value μ in this scenario (marked in red in Figure 21b) is approximately 30% lower than under low torque conditions (e.g., third braking maneuver of Bahrain laps). The complex tribological behavior of C/C composites is investigated in the literature for aeronautical applications primarily as a function of ambient conditions and adsorption effects, applied load, speed, temperature, type of carbon matrix and fibers, and heat treatment temperature of the composites [27–44]. In the literature, no studies have been found that specifically address the tribological behavior of C/C composites used for race vehicles, which may differ in terms of manufacturing process, resulting material properties, and operating conditions. However, according to available studies, at higher braking pressures, wear debris is extruded and coated on the friction surface to form a compact and smooth friction film, resulting in a lower coefficient of friction [30–32,37,38]. Therefore, it is deemed reasonable to attribute this observed behavior under high torque conditions to the tribological characteristics of C/C.

The simulation of the same braking maneuver is compared with the experimental data in Figure 22. The model provides highly accurate torque predictions under these severe operating conditions, replicating the peak torque and the minimum friction value during pressure modulation with errors of 1% and 3%, respectively.

On average, the experimental peak torque measured for caliper C is nominally equivalent to that of caliper A [15] (i.e., −1.5% for the amplified caliper), but it is achieved at a hydraulic pressure of 4.5% lower. Once the gain coefficient μ_g and the effective friction μ—whether experimental or simulated—are calculated according to Equations (4) and (5),

it is possible to estimate the effective mean contact pressure $p_{c,eff}$ (i.e., including the wedge effect) as described in Equation (18).

$$p_{c,eff} = \frac{BT}{2\mu R_{eff} A_{pad}} \tag{18}$$

In the peak torque condition, caliper A exhibits an effective friction coefficient μ approximately 4% higher than caliper C, which is attributable to an effective mean contact pressure $p_{c,eff}$ 13% lower for caliper A compared to amplified caliper C.

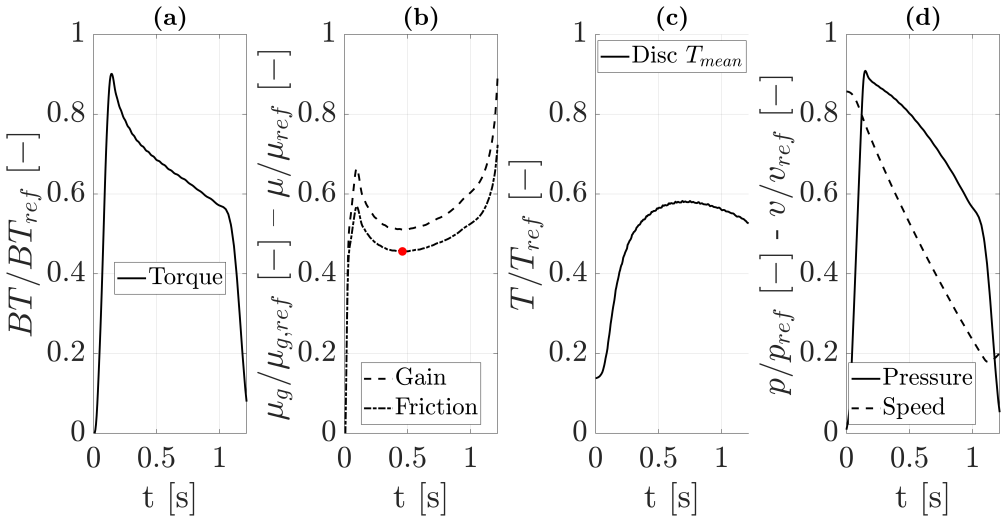

Figure 21. Experimental results of an individual braking maneuver from a high torque cycle (high p_{max}) of caliper C (27°): (**a**) braking torque, (**b**) gain coefficient μ_g and effective friction μ, (**c**) disc surface temperature, (**d**) hydraulic pressure and vehicle speed.

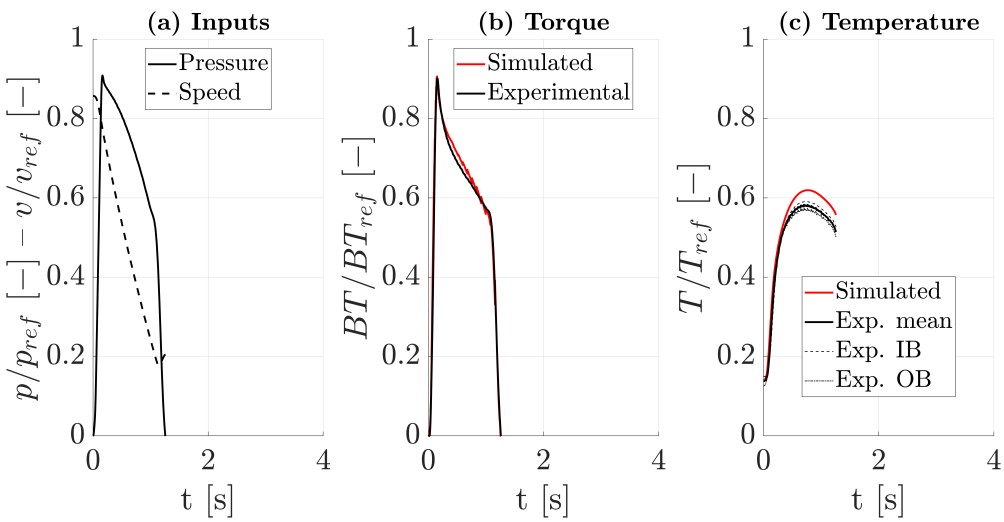

Figure 22. Simulation of an individual braking maneuver from a high torque cycle (high p_{max}) of caliper C (27°).

The mean error indices of the simulations performed for caliper C are summarized in Table 7. Temperature rmse values remain below 50 °C, and normalized peak torque errors below 5% are obtained.

Table 7. Mean error indices of the test cycles simulated for caliper C (27°)—braking maneuvers simulated individually.

Cycle	Notes	N	Mean Error Indices							
			ET_{rmse} [°C]	ET_{nrmse} [%]	ET_{peak} [°C]	ET_{npeak} [%]	EC_{rmse} [N m]	EC_{nrmse} [%]	EC_{peak} [N m]	EC_{npeak} [%]
BAH	Low T_0	16	16.2	6.7	11.5	2.1	127.9	5.2	98.0	4.5
BAH	Mid T_0	8	15.2	5.3	13.8	1.9	145.6	5.8	88.8	4.4
BAH	High T_0	8	24.6	9.0	28.8	3.6	132.0	5.4	80.6	3.7
HT	Low p_{max}	5	29.0	6.8	37.8	6.7	146.2	3.1	128.9	2.8
HT	Mid p_{max}	5	31.5	7.3	39.7	7.0	147.7	3.0	107.7	2.2
HT	High p_{max}	3	32.8	7.4	39.7	6.9	148.4	2.9	94.8	1.8

3.1.3. Validation of Caliper D

Caliper D is a prototype of a front F1 braking system developed in 2024, designed with a high wedge angle of $\beta = 40°$. As shown in Figure 12d and Table 2, this braking system shares the same caliper body as caliper C, but is equipped with different pads and pad supports to achieve the required variation of the wedge angle. As for caliper C, this configuration is a prototype and has not been used in on-track applications.

Figure 23 illustrates the simulation of a Bahrain cycle lap at high initial temperature T_0. As reported in Table 8, the mean torque error indices for the eight braking phases of the lap are 4.6% for the nrmse index and 6.5% for the npeak index. In particular, the model shows an 8% overestimation of the peak braking torque for the first and most demanding braking maneuver. In the same condition, errors below 4% and 1% were obtained for caliper C and caliper B and A, respectively. The same error index for caliper D is reduced below 4% for the first braking phase of Bahrain cycles run in lower temperature regimes.

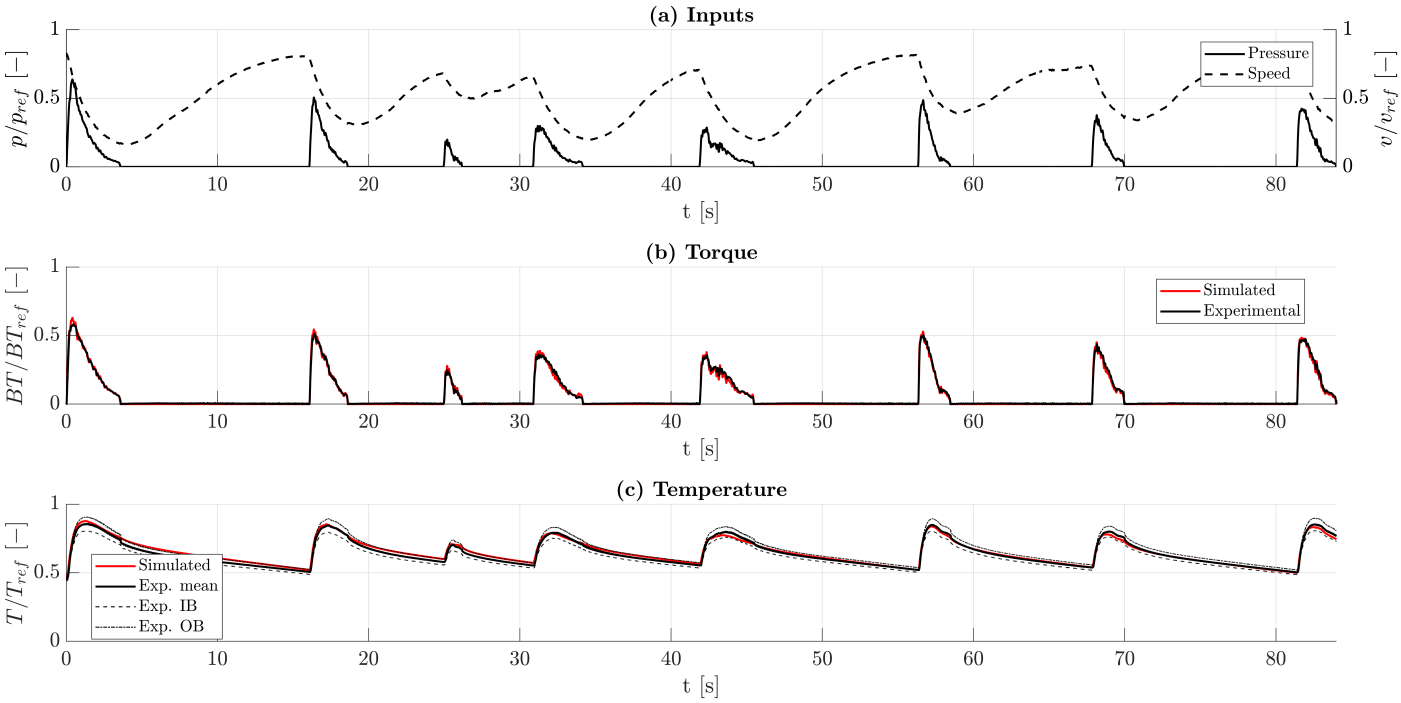

Figure 23. Bahrain cycle full lap simulation of caliper D (40°)—pressure and speed inputs—high starting temperature cycle.

The analysis of the experimental results obtained for high temperature Bahrain cycles highlights the high efficiency of caliper D in low demanding torque conditions, as they

imply lower mean effective contact pressure and therefore higher values of mean effective friction coefficient. This finding is most pronounced for the third braking maneuver of the lap, with caliper D requiring a maximum hydraulic pressure 17% and 22% lower than caliper C ($\beta = 27°$) and caliper B ($\beta = 20°$), respectively, to deliver the same torque (note that these three calipers feature the same total piston area A_{pist} and comparable values of effective radius R_{eff}). This result is consistent with Equations (4) and (5) evaluated assuming $\mu \simeq 0.5$ (i.e., theoretically predicting a maximum hydraulic pressure for caliper D 15.6% and 23.5% lower than cases C and B, respectively). In contrast, the most demanding torque conditions show close values of experimental maximum hydraulic pressure for caliper D and caliper C in this temperature regime, due to the reduction of friction induced by the higher $p_{c,eff}$ and by the extreme local contact pressures in the wedge region for the most amplified caliper.

The last scenario analyzed for caliper D is a braking maneuver from a high torque cycle at the highest pressure level applied. The experimental results obtained are presented in Figure 24. Compared to the same condition analyzed for caliper C (Figure 21 in Section 3.1.2), the following findings are derived.

- caliper D delivers nominally the same peak torque (−2%) as caliper C, at a peak hydraulic pressure approximately 5% lower.
- The effective friction coefficient of caliper D at maximum torque is 7% and 10.5% lower than caliper C ($\beta = 27°$) and A (standard), respectively.
- The maximum effective mean contact pressure $p_{c,eff}$ of caliper D is 11% and 28% larger than caliper C ($\beta = 27°$) and A (standard), respectively.
- The minimum friction coefficient of caliper D during pressure modulation (marked in red in Figure 24b) is 2.3% and 5.6% lower than caliper C ($\beta = 27°$) and A (standard), respectively.

If the same effective friction μ recorded at maximum torque for $\beta = 27°$ yielded for caliper D, the same peak torque would be achieved at a hydraulic pressure 12% lower than that measured for caliper C. The experimental outcomes obtained for high torque cycles align with the findings of Bahrain cycles and therefore confirm the deterioration of the effective friction coefficient μ as contact pressures increase [30,31,37,38].

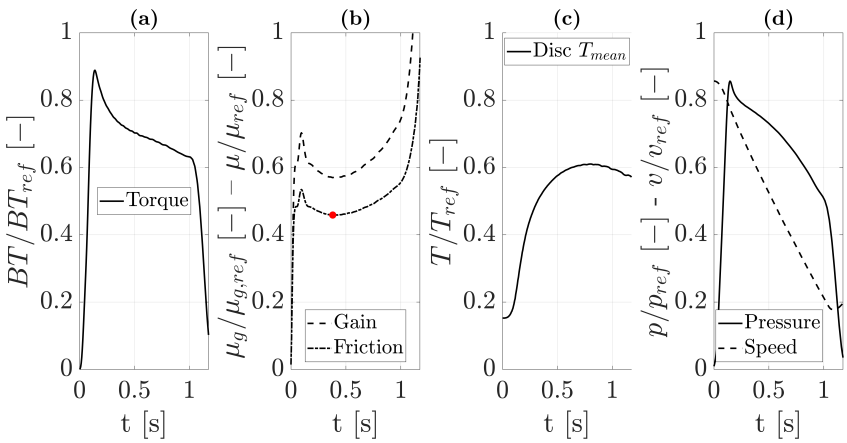

Figure 24. Experimental results of an individual braking maneuver from a high torque cycle (high p_{max}) of caliper D (40°): (**a**) braking torque, (**b**) gain coefficient μ_g and effective friction μ, (**c**) disc surface temperature, (**d**) hydraulic pressure and vehicle speed.

Figure 25 shows the simulation results of the same braking maneuver. The model provides a satisfactory prediction of torque under this condition, with an error index npeak of 2.4% and a nrmse of 6.2% (see Table 8). The latter is attributed to the torque

underestimation observed during the final phase of pressure application, during which a steep increase in experimental friction is observed (Figure 24b).

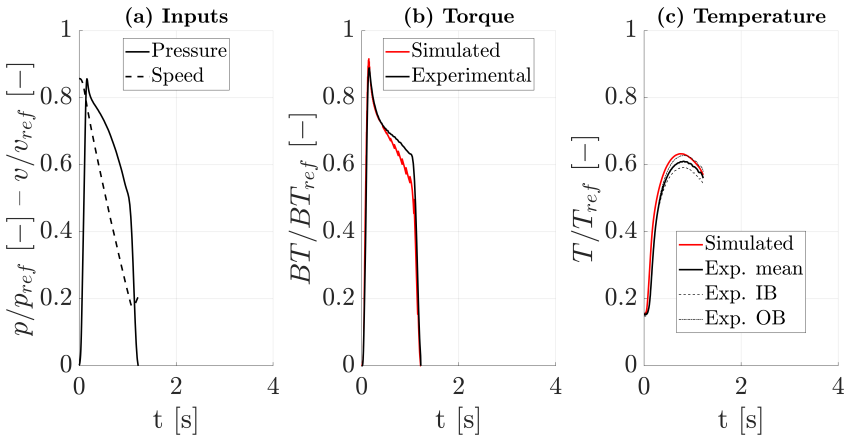

Figure 25. Simulation of an individual braking maneuver from a high torque cycle (high p_{max}) of caliper D (40°).

Table 8. Mean error indices of the test cycles simulated for caliper D (40°)—braking maneuvers simulated individually.

Cycle	Notes	N	Mean Error Indices							
			ET_{rmse} [°C]	ET_{nrmse} [%]	ET_{peak} [°C]	ET_{npeak} [%]	EC_{rmse} [N m]	EC_{nrmse} [%]	EC_{peak} [N m]	EC_{npeak} [%]
BAH	Low T_0	8	25.8	9.2	19.1	2.9	213.5	8.5	148.0	6.8
BAH	Mid T_0	24	27.8	9.8	29.6	4.1	162.1	6.6	70.4	3.0
BAH	High T_0	8	19.5	7.3	19.5	2.4	110.1	4.6	155.6	6.5
HT	Low p_{max}	5	34.7	7.8	16.2	2.7	212.2	4.5	190.6	4.0
HT	Mid p_{max}	5	43.9	9.7	15.8	2.6	288.4	5.8	107.9	2.2
HT	High p_{max}	5	49.3	10.8	20.5	3.4	324.0	6.2	126.7	2.4

3.2. Model as Preliminary Design Tool

After being validated in a wide range of configurations and test cycles, the thermoelastic model is used as a tool for the preliminary evaluation of the performance of a new prototype front braking system (shown in Figure 12e), compliant with F1 technical regulations. As the caliper geometry has already been defined, all necessary geometric inputs for the model—such as piston dimension and layout, wedge angle, and disc and pad geometry—are directly available from the CAD models. At this stage, no experimental test bench data are available, as this braking system—hereafter referred to as caliper X—has not yet been tested. The key design features of this prototype, summarized in Table 2, include a high wedge angle ($\beta = 40°$), a reduced number of pistons (two per side, instead of three), and an increased pad contact area—6% and 12% larger than those of calipers C and D, respectively.

Assuming a reference effective friction coefficient $\mu = 0.45$, and based on the geometry of the system along with Equations (4) and (5), configuration X is theoretically expected to deliver the same braking torque as caliper C ($\beta = 27°$), while offering a significant weight reduction of 21%—calculated on the combined mass of the caliper body and pistons.

To virtually assess braking performance, dedicated simulations have been carried out. Figures 26 and 27 show the results of the first braking maneuver of a Bahrain lap at low and high initial disc temperatures T_0, respectively. Unlike the simulations presented in previous sections, the input data consist here of the target torque and disc speed time

histories; therefore, the hydraulic pressure is computed as an output. This is made possible by using the inverse version of the thermoelastic model [14,15].

In both scenarios, the simulated hydraulic pressure profile for caliper X closely matches that of caliper C, in agreement with theoretical expectations. The maximum observed deviation in peak pressure—3% higher for caliper X—occurs in the high temperature scenario illustrated in Figure 27. For reference, experimental bench data from caliper C are also included to evaluate the accuracy of its corresponding simulations.

Figure 28 presents the simulation of a braking maneuver from a high torque cycle, providing the hydraulic pressure time history as input. The disc angular speed time history is not imposed, but is simulated by integrating the angular deceleration $\dot{\omega}$ in time. The angular deceleration is evaluated according to Equation (19) as the ratio of the simulated braking torque BT to the total mechanical moment of inertia I.

$$\omega(t) = \int_0^t \dot{\omega}(\tau)d\tau + \omega_0 = \int_0^t -\frac{BT(\tau)}{I}d\tau + \omega_0 \tag{19}$$

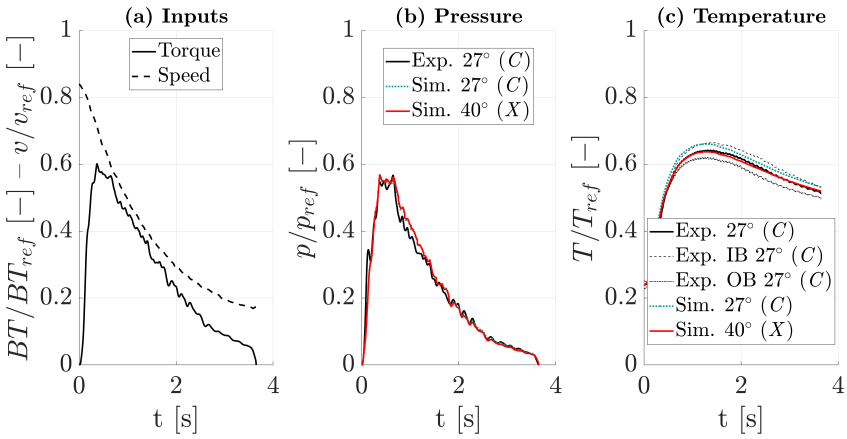

Figure 26. Simulation of the first braking maneuver of a Bahrain cycle at low starting temperature T_0, providing braking torque and speed as simulation input (i.e., inverse model version)—caliper C (27°) and X (40°—4 piston layout).

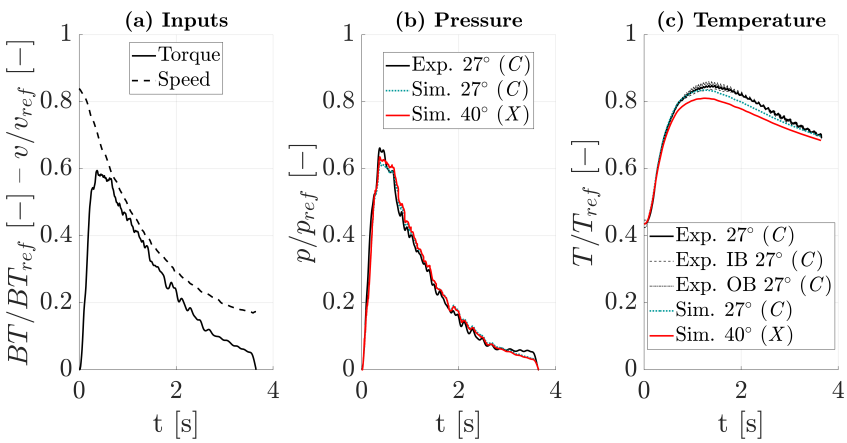

Figure 27. Simulation of the first braking maneuver of a Bahrain cycle at high starting temperature T_0, providing braking torque and speed as simulation input (i.e., inverse model version)—caliper C (27°) and X (40°—4 piston layout).

The same braking maneuver previously analyzed in Figure 22 is simulated here for caliper X. The performance simulated closely matches that of its reference configuration also in this severe braking scenario. Despite the larger wedge angle that implies higher local contact pressures in the wedge region, this result is achieved thanks to a contact

area A_{pad} 6% larger than for caliper C. This reflects on a lower mean effective pressure $p_{c,eff}$ for caliper X (−5%) and close values of effective friction μ for the two calipers at the time instant of maximum torque. Based on the validation performed for the other configurations, the highest prediction accuracy for caliper X is expected in terms of peak torque estimation, whereas a greater variability in friction behavior may occur during the final phase of pressure application.

Finally, after simulating a complete mapping cycle using the same modeling approach adopted for the high torque scenario, the virtual friction map of braking system X is generated. The result is shown in Figure 29, where the gain coefficient μ_g is compared to the theoretical effective friction coefficient μ. As for experimental friction maps, virtual maps can then be used in combination with full vehicle models and lumped parameter thermal models of the discs (i.e., co-simulation environment) in order to assess the impact of the braking system on the vehicle performance.

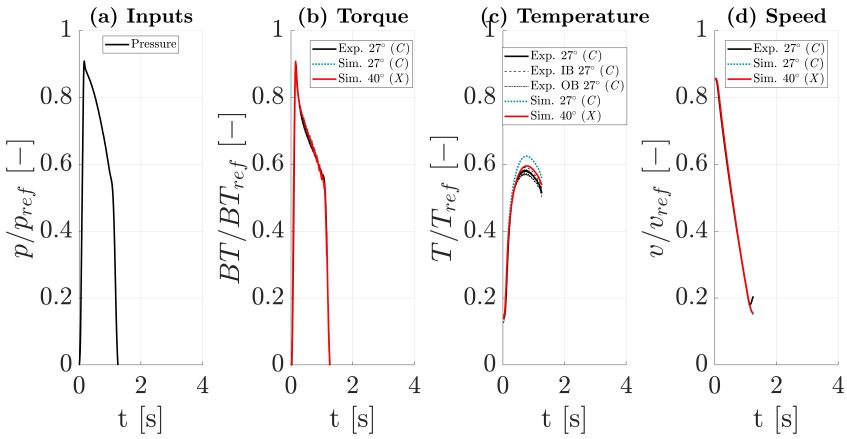

Figure 28. Simulation of a braking maneuver of a high torque cycle (high p_{max}), providing hydraulic pressure and initial speed as simulation input (i.e., model version with imposed inertia I)—caliper C (27°) and X (40°—4 piston layout).

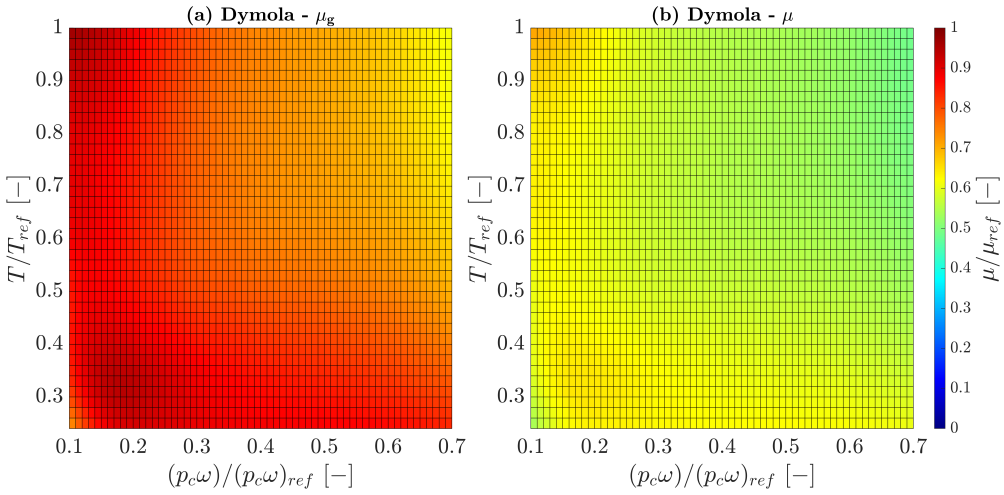

Figure 29. Virtual friction maps of caliper X (40°—4 piston layout). (**a**) Gain coefficient μ_g (**b**) Effective friction coefficient μ.

4. Conclusions

This work presents a modeling strategy that aims to predict the performance of wedge-amplified C/C braking systems in high-performance racing applications. A simplified equilibrium model for a wedged brake pad is introduced, from which an analytical expres-

sion is derived to describe the nonlinear dependence of the gain coefficient on both the wedge angle and the mean effective friction coefficient.

The coupled thermoelastic FVM model built in Dymola is adapted to simulate wedge-amplified calipers. Several simulations of different test cycles performed on a dyno are run, and the predicted braking torque and disc surface temperature are compared against experimental data to evaluate the model accuracy.

The analysis of experimental dyno data of the different braking systems leads to the following key findings.

- A temperature-induced reduction of friction is observed in Bahrain cycles performed in higher temperature scenarios, in agreement with the findings analyzed in previous work for the non-amplified caliper layout.
- A decrease in the effective friction coefficient with increasing mean effective contact pressure—trend especially pronounced in configurations with high wedge angles and reduced pad contact areas. As a result, in high torque scenarios, higher hydraulic pressures are required than theoretical estimates would suggest, due to the reduction in effective friction compared to standard or low-amplified configurations.
- High-amplified configurations are most efficient in low torque scenarios, as they imply working at low mean effective contact pressure and high effective friction.

Overall, the local friction law embedded in the model successfully captures this behavior. The model consistently yields mean rmse indices below 50 °C for temperature prediction, while the error indices nrmse and npeak for torque prediction remain below 5% for the majority of the configurations tested, never exceeding 10%.

The validated model is applied to predict the performance of a new caliper (caliper X), not yet experimentally tested, designed to deliver the same theoretical braking torque at the same hydraulic pressure as an existing reference braking system (caliper C). The agreement with both the simulated and experimental results of caliper C suggests the capability of the model as a tool to evaluate the braking performance of early-stage designs, based on their geometry, hydraulic layout, and wedge angle.

Future work will focus on refining the model through a dedicated experimental investigation of the local tribological behavior of C/C materials, especially under high contact pressures induced by large wedge angles. Pin-on-disc tribometer testing is expected to improve the characterization of local friction behavior and dynamics, thus possibly further enhancing the predictive capability of the model.

Author Contributions: Conceptualization, G.G., M.G. and G.M.; methodology, G.G., M.G. and R.P.; software, G.G.; validation, G.G., C.C. and R.P.; formal analysis, M.G., G.M. and C.C.; investigation, G.G., M.G. and R.P.; resources, C.C. and R.P.; data curation, G.G.; writing—original draft preparation, G.G.; writing—review and editing, M.G., G.M., C.C. and R.P.; visualization, G.G.; supervision, M.G., G.M., C.C. and R.P.; project administration, M.G., G.M., C.C. and R.P.; funding acquisition, M.G., G.M., C.C. and R.P. All authors have read and agreed to the published version of the manuscript.

Funding: This research received no external funding.

Data Availability Statement: The authors confirm that the data supporting the findings of this study are available within the article.

Conflicts of Interest: Authors Carlo Cantoni and Raffaello Passoni were employed by the company Brembo (Italy). The remaining authors declare that the research was conducted in the absence of any commercial or financial relationships that could be construed as a potential conflict of interest.

Nomenclature

C/C	Carbon-carbon
C/C	Carbon-carbon
ICE	Internal combustion engine
HEVs	Hybrid electric vehicles
EVs	Electric vehicles
EWB	Electronic wedge brake
EMB	Electromechanical brake
PMSM	Permanent magnet synchronous motor
ADRC	Active disturbance rejection control
MR	Magnetorheological
F1	Formula One
CVI	Chemical vapor infiltration
FVM	Finite volume method
FEM	Finite element method
FEA	Finite element analysis
CAE	Computer-aided engineering
2D	Three-dimensional
3D	Three-dimensional
CAD	Computer-aided design
CNS	Contact normal stress
SVVR	Solid to void volume ratios
SVSR	Solid to void surface ratios
CFD	Computational fluid dynamics
HTC	Heat transfer coefficient
MAP	Mapping cycle
BAH	Bahrain cycle
HD	Heavy duty cycle
HT	High torque cycle
IB	Inboard disc side
OB	Outboard disc side
α	Wedge angle [°]
F_m	Actuation force [N]
F_b	Tangential braking force [N]
$F_{z,disc}$	Normal reaction force on the disc-pad contact surface [N]
$F_{f,w}$	Friction force on the wedge surface [N]
$F_{z,pist}$	Hydraulic force applied by pistons [N]
$F_{f,pist}$	Friction force between pad and pistons [N]
F_n	Normal reaction force on the wedge surface [N]
μ	Friction coefficient (uniform) on the disc-pad contact surface [-]
μ_w	Friction coefficient on the pad-wedge contact surface [-]
μ_p	Friction coefficient on the pad-piston contact surfaces [-]
β	Wedge angle (complementary to α) [°]
μ_g	Gain coefficient (i.e., global friction coefficient) of the braking system [-]
BT	Braking torque [N m]
p_{hydr}	Hydraulic pressure [Pa]
A_{pist}	Total area of pistons (per caliper side) facing the brake fluid [m^2]
R_{eff}	Caliper effective radius [m]
R_w	Wheel radius [m]
μ_l	Local friction coefficient [-]
p_l	Local contact pressure [Pa]

v_l	Local sliding speed [m/s]
T_l	Local temperature in contact submodel [K]
d_i	Coefficient of the i-th term of the friction law
f_i	i-th function of the friction law
ω	Disc angular speed [rad/s]
u_n	Pad displacement along the n direction (i.e., normal to the wedge) [m]
u_s	Pad displacement along the s direction (i.e., horizontal) [m]
$u_{i,BC}$	Boundary displacement along direction $i = r, \theta, z$ (local reference system) in the tangential loaded boundary region of the pad [m]
γ	Tangential coordinate of the pad boundary surface [rad]
φ	Pad angular amplitude [rad]
k_{BC}	Penalty stiffness [N/m]
$F_{f,a}$	Axial component of the total friction force on the wedge surface [N]
$F_{f,v}$	Vertical component of the total friction force on the wedge surface [N]
F_s	Reaction force on the wedge along the s direction (i.e., horizontal) [N]
$F_{i,BC}$	Boundary force along direction $i = r, \theta, z$ (local reference system) in the tangential loaded boundary region of the pad [N]
A_{pad}	Actual pad contact area [m^2]
d_e	Disc external diameter [m]
t_d	Disc thickness [m]
t_p	Pad thickness [m]
p_c	Mean contact pressure (without wedge contribution) [Pa]
T_0	Initial temperature of the cycle [°C]
$EC_{(),j}$	Torque error index (rmse, nrmse, peak, npeak) of braking maneuver j
$ET_{(),j}$	Temperature error index (rmse, nrmse, peak, npeak) of braking maneuver j
$p_{c,eff}$	Mean effective contact pressure (with wedge contribution) [Pa]
$\dot{\omega}$	Disc angular deceleration [rad/s^2]
ω_0	Disc initial angular speed [rad/s]
I	Total bench moment of inertia [kg m^2]

References

1. Cantoni, C.M.D.; Cesarini, R.; Mastinu, G.R.; Previati, G.; Sicigliano, R. Brake system dynamics. In *Road and Off-Road Vehicle System Dynamics Handbook*; CRC Press: Boca Raton, FL, USA, 2014; pp. 837–917.
2. *ISO 611:2003*; Road Vehicles–Braking of Automotive Vehicles and Their Trailers–Vocabulary. International Organization for Standardization: Geneva, Switzerland, 2003.
3. Guarneri, P.; Mastinu, G.; Gobbi, M.; Cantoni, C.; Sicigliano, R. Brake Energy Efficiency. *J. Mech. Des.* **2014**, *136*, 081001. [CrossRef]
4. Hartmann, H.; Schautt, M.; Pascucci, A.; Gombert, B. *eBrake®-the Mechatronic Wedge Brake*; SAE Transactions: New York, NY, USA, 2002; pp. 2146–2151.
5. Jing, H.; Lin, Q.; Liu, M.; Liu, H. Electromechanical braking systems and control technology: A survey and practice. *Proc. Inst. Mech. Eng. D* **2025**, *239*, 4551–4573. [CrossRef]
6. Balogh, L.; Stréli, T.; Németh, H.; Palkovics, L. Modelling and simulating of self-energizing brake system. *Veh. Syst. Dyn.* **2006**, *44*, 368–377. [CrossRef]
7. Han, K.; Kim, M.; Huh, K. Modeling and control of an electronic wedge brake. *Proc. Inst. Mech. Eng. C* **2012**, *226*, 2440–2455. [CrossRef]
8. Ivanov, V.A.; Ayalew, B. Adjustable Electromechanical Wedge Brakes with Reduced Energy Consumption. In Proceedings of the ASME 2011 International Mechanical Engineering Congress and Exposition, Denver, CO, USA, 11–17 November 2011; Volume 9, pp. 179–186. [CrossRef]
9. Xu, F.; Cho, C. A Novel Electronic Wedge Brake Based on Active Disturbance Rejection Control. *Energies* **2022**, *15*, 5096. [CrossRef]
10. Yan, Z.; Peng, H.; Chen, X.; Yan, M. Design, Modeling, and Control of Electronic Mechanical Brake System: A Review. *SAE Int. J. Veh. Dyn. Stab. NVH* **2024**, *08*, 467–489. [CrossRef]
11. Yu, L.; Ma, L.; Song, J.; Liu, X. Magnetorheological and Wedge Mechanism-Based Brake-by-Wire System with Self-Energizing and Self-Powered Capability by Brake Energy Harvesting. *IEEE/ASME Trans. Mechatron.* **2016**, *21*, 2568–2580. [CrossRef]

12. Wang, J.; Yang, N.; Wang, Z.; Yang, Y.; Chu, L. Design and Simulation of a Novel Wedge Disc Brake. In *Proceedings of the FISITA 2012 World Automotive Congress*; SAE-China; FISITA; Springer: Berlin/Heidelberg, Germany, 2013; Volume 198, pp. 95–104, Series Title: Lecture Notes in Electrical Engineering. [CrossRef]
13. Wang, J.; Zhang, Y.; Yang, N.; Song, D.; Wang, Q. Parameters design and braking efficiency analysis of a hydraulic self-energizing wedge disc brake. *Int. J. Precis. Eng. Manuf.* **2017**, *18*, 1409–1418. [CrossRef]
14. Galvanini, G.; Gobbi, M.; Mastinu, G.; Cantoni, C.; Passoni, R. Thermoelastic modeling of high-performance carbon–carbon (C/C) brakes. *Therm. Sci. Eng. Prog.* **2025**, *63*, 103664. [CrossRef]
15. Galvanini, G.; Gobbi, M.; Mastinu, G.; Cantoni, C.; Passoni, R. Extended validation of a thermoelastic model for carbon-carbon (C/C) brake systems in high-performance racing applications. *Therm. Sci. Eng. Prog.* **2026**, *69*, 104467. [CrossRef]
16. Gobbi, M.; Mastinu, G.; Previati, G.; Cantoni, C.; Passoni, R. Thermo-Elastic Modelling of High Performance Braking Systems. In Proceedings of the ASME 2016 DETC, Charlotte, NC, USA, 21–24 August 2016; number DETC2016-59996, p. V003T01A023. [CrossRef]
17. 2025 Formula 1 Technical Regulations. 2025. Available online: https://www.fia.com/regulation/category/110 (accessed on 27 October 2025).
18. Cividini, O.; Passoni, R. Brake Systems and Composite Rotors: How Racing can be a Vision for High Performance Cars. *SAE Int. J. Adv. Curr. Prac. Mobil.* **2022**, *5*, 1379–1386. [CrossRef]
19. Wong, J.Y. *Theory of Ground Vehicles*; John Wiley & Sons: Hoboken, NJ, USA, 2022.
20. TecSA TC 225. 2026. Available online: https://www.tecsa-srl.it/car-test-bench-225/ (accessed on 5 March 2026).
21. Texense-INF-T 1000-V2. 2025. Available online: https://www.texense.com/it/sensors/inf-t-it/ (accessed on 5 March 2026).
22. Modelica®—A Unified Object-Oriented Language for Systems Modeling. Language Specification. 2023. Available online: https://specification.modelica.org/maint/3.6/MLS.pdf (accessed on 5 March 2026).
23. Dassault Systèmes. *Dymola, Dynamic Modeling Laboratory, User Manual 1A: Introduction, Getting Started, and Installation*, 2021.
24. Dymola-Multi-Engineering Modeling and Simulation based on Modelica and FMI. 2024. Available online: https://www.3ds.com/products/catia/dymola (accessed on 5 March 2026).
25. Kim, E.; Yashiki, T.; Suzuki, F.; Katagiri, Y.; Yoshida, T. Thermal deformation analysis using modelica. In Proceedings of the The first Japanese Modelica Conference, Tokyo, Japan, 23–24 May 2016; pp. 121–128. [CrossRef]
26. Lee, K. Numerical Prediction of Brake Fluid Temperature Rise During Braking and Heat Soaking. In *SAE Technical Paper*; SAE: New York, NY, USA, 1999; number 1999-01-0483. [CrossRef]
27. Kasem, H.; Bonnamy, S.; Berthier, Y.; Jacquemard, P. Characterization of surface grooves and scratches induced by friction of C/C composites at low and high temperatures. *Tribol. Int.* **2010**, *43*, 1951–1959. [CrossRef]
28. Lei, B.; He, L.; Yi, M.; Ran, L.; Xu, H.; Ge, Y.; Peng, K. New insights into the microstructure of the friction surface layer of C/C composites. *Carbon* **2011**, *49*, 4554–4562. [CrossRef]
29. Wu, S.; Liu, Y.; Ge, Y.; Ran, L.; Peng, K.; Yi, M. Structural transformation of carbon/carbon composites for aircraft brake pairs in the braking process. *Tribol. Int.* **2016**, *102*, 497–506. [CrossRef]
30. Gao, Z.; Yuan, Z.; Yang, Y.; Li, Z.; Huang, B. Microstructural transformation impact on mechanical and tribological performance of different temperature heat-treated carbon/carbon composites. *Ceram. Int.* **2024**, *50*, 36099–36111. [CrossRef]
31. Yen, B.; Ishihara, T. On temperature-dependent tribological regimes and oxidation of carbon-carbon composites up to 1800 °C. *Wear* **1996**, *196*, 254–262. [CrossRef]
32. Yen, B.; Ishihara, T. An investigation of friction and wear mechanisms of carbon-carbon composites in nitrogen and air at elevated temperatures. *Carbon* **1996**, *34*, 489–498. [CrossRef]
33. Yen, B.; Ishihara, T.; Yamamoto, I. Influence of environment and temperature on "dusting" wear transitions of carbon–carbon composites. *J. Mater. Sci.* **1997**, *32*, 681–686. [CrossRef]
34. Gomes, J.; Silva, O.; Silva, C.; Pardini, L.; Silva, R. The effect of sliding speed and temperature on the tribological behaviour of carbon–carbon composites. *Wear* **2001**, *249*, 240–245. [CrossRef]
35. Gouider, M.; Berthier, Y.; Jacquemard, P.; Rousseau, B.; Bonnamy, S.; Estrade-Szwarckopf, H. Mass spectrometry during C/C composite friction: Carbon oxidation associated with high friction coefficient and high wear rate. *Wear* **2004**, *256*, 1082–1087. [CrossRef]
36. Tanner, J.A.; Travis, M. *Adsorption and Desorption Effects on Carbon Brake Material Friction and Wear Characteristics*; SAE transactions: New York, NY, USA, 2005; pp. 1517–1534.
37. Xiong, X.; Li, J.H.; Huang, B.Y. Impact of brake pressure on the friction and wear of carbon/carbon composites. *Carbon* **2007**, *45*, 2692–2694. [CrossRef]
38. Deng, H.; Li, K.; Li, H.; Wang, P.; Xie, J.; Zhang, L. Effect of brake pressure and brake speed on the tribological properties of carbon/carbon composites with different pyrocarbon textures. *Wear* **2010**, *270*, 95–103. [CrossRef]
39. Shu, Y.; Jie, C.; Qizhong, H.; Xiang, X.; Tong, C.; Yunping, L. Effect of Braking Speeds on the Tribological Properties of Carbon/Carbon Composites. *Mater. Trans.* **2010**, *51*, 1038–1043. [CrossRef]

40. Yu, S.; Zhang, F.; Xiong, X.; Li, Y.; Tang, N.; Koizumi, Y.; Chiba, A. Tribological properties of carbon/carbon composites with various pyrolytic carbon microstructures. *Wear* **2013**, *304*, 103–108. [CrossRef]
41. Wu, S.; Yi, M.; Ge, Y.; Ran, L.; Peng, K. Effect of carbon fiber reinforcement on the tribological performance and behavior of aircraft carbon brake discs. *Carbon* **2017**, *117*, 279–292. [CrossRef]
42. Sharma, A.; Sadeghi, F.; Glen, S.; Murdie, N.; Shula, B. Friction & wear characteristics of pitch & poly-acrylonitrile based carbon-carbon composites in air and nitrogen environment under aircraft taxi conditions. *Tribol. Int.* **2022**, *174*, 107729. [CrossRef]
43. Shpenev, A.; Muravyeva, T.; Shkalei, I.; Bukovskiy, P. Influence of the Surface Film (Third Body) on the Friction and Wear Process of Carbon-Fiber Composites. *J. Surf. Investig. X-Ray Synchrotron Neutron Tech.* **2022**, *16*, 397–401. [CrossRef]
44. Bukovskiy, P.; Morozov, A.; Kulakov, V.; Golubkov, A.; Rodionov, N.; Kirichenko, A. High-Temperature Tribotechnical Properties of Carbon–Carbon Friction Composites. *J. Frict. Wear* **2022**, *43*, 322–329. [CrossRef]

Disclaimer/Publisher's Note: The statements, opinions and data contained in all publications are solely those of the individual author(s) and contributor(s) and not of MDPI and/or the editor(s). MDPI and/or the editor(s) disclaim responsibility for any injury to people or property resulting from any ideas, methods, instructions or products referred to in the content.